Spectral performance analysis of the Fizeau interferometer on board ESA's Aeolus wind lidar satellite

Michael Vaughan[1], **Kevin Ridley**[2], **Benjamin Witschas**[3], **Oliver Lux**[3], **Ines Nikolaus**[4], and **Oliver Reitebuch**[3]

[1]Optical & Lidar Associates OLA, Buckinghamshire, UK
[2]Department of Physics and Astronomy, University of Birmingham, Birmingham, UK
[3]Institut für Physik der Atmosphäre, Deutsches Zentrum für Luft- und Raumfahrt e.V. (DLR), 82234 Oberpfaffenhofen, Germany
[4]Department of Applied Sciences and Mechatronics, University of Applied Sciences Munich, Munich, Germany

Correspondence: Benjamin Witschas (benjamin.witschas@dlr.de)

Abstract. This paper presents an extensive investigation of the signal fringe profile for the Fizeau interferometer used in the first spaceborne wind lidar Aeolus and considers the fundamental implications for the wind measurement accuracy in Aeolus and future systems. The early Aeolus design phase considered that the basic fringe would be made up of a Fizeau instrumental component of $\approx 100\,\mathrm{MHz}$ (full width at half maximum, FWHM), folded with the laser pulse spectral width of $\approx 50\,\mathrm{MHz}$ (FWHM), both of Lorentzian form. Fringe anomalies observed before the mission and related to surface defects in the interferometer plates triggered the development of wave-optic methods for analysis of the fringe formation. These methods, herein described in an instructional appendix, were subsequently found to be essential for rigorous modelling of complex fringes for different physical and optical arrangements. Initial signal returns from Aeolus suggested that the Fizeau fringe profile was in fact broadened with a large Gaussian component. The laser pulse was subsequently shown to have a profile close to Gaussian of $\approx 45\,\mathrm{MHz}$ (FWHM) and thus provided a partial contribution. However, detailed examination of experimental Aeolus fringes constructed from ground return signals showed a large Gaussian component up to $\approx 130\,\mathrm{MHz}$ (FWHM). Wave-optic modelling established that Fizeau "aperture broadening", of this form and magnitude, would be generated for the input signal beam of $500\,\mu\mathrm{rad}$ field of view (FOV) set at a large angle of incidence (AOI) of $300\,\mu\mathrm{rad}$. These findings have strong implications for fringe shift and wind measurement accuracy, as given in the quantum-limited Cramér–Rao expression and the paramount importance of minimizing line width. Extensive modelling and simulation for the broadened profiles calculated above shows good agreement with measured Aeolus global wind measurement accuracies and indicates that loss of signal could be due to beam clipping at the field stop for such a large AOI. It is established that optimization of the present Aeolus Fizeau parameters could lead to a factor of 2.5 improvement in wind measurement precision. Future upgrades of the Fizeau interferometer and the laser within reasonable parameters suggest the potential for a factor of 7.6 improvement on the in-orbit performance.

1 Introduction

On 22 August 2018, the European Space Agency (ESA) launched the first-ever spaceborne Doppler wind lidar, Aeolus, into a sun-synchronous orbit at about $320\,\mathrm{km}$ altitude, with an orbit repeat cycle of $7\,\mathrm{d}$ (ESA, 2008; Schillinger et al., 2003). Aeolus carried the Atmospheric Laser Doppler Instrument (ALADIN) as a single payload and operated successfully until April 2023 while additional instrument tests were performed until the completion of the mission in July 2023. ALADIN provided global profiles of the wind component along the instrument's line-of-sight (LOS) direction from the ground up to about $30\,\mathrm{km}$ altitude (ESA, 1999; Stoffelen et al., 2005; Reitebuch, 2012; Kanitz et al., 2019; Reitebuch et al., 2020; Straume et al., 2020), mainly

aiming to improve numerical weather prediction (NWP) and medium-range weather forecasts (Weissmann and Cardinali, 2007; Tan et al., 2007; Marseille et al., 2008; Horányi et al., 2015; Rennie et al., 2021). Especially wind profiles acquired over the Southern Hemisphere, the tropics, and the oceans contribute to closing gaps in the availability of global wind data, which represented a major deficiency in the global observing system before the launch of Aeolus (Baker et al., 2014).

For the use of Aeolus observations in NWP models, a detailed characterization of the data quality as well as the minimization of systematic errors is crucial. Thus, several scientific and technical studies have been performed and published in the meantime, addressing the performance of ALADIN and the quality of the Aeolus data products. In particular, NWP model data (Rennie et al., 2021), airborne wind lidar measurements (Lux et al., 2020, 2022; Witschas et al., 2020, 2022a), radiosonde observations (Martin et al., 2021; Baars et al., 2020; Borne et al., 2024), and various different ground-based instruments have been used to characterize the quality of Aeolus horizontal LOS winds for different periods, different geolocations, and different data products. In addition to that, the ALADIN instrument performance in space was characterized by investigating the laser frequency stability (Lux et al., 2021), the spectral performance of the Fabry–Perot interferometers used to measure wind from the light backscattered from molecules (Witschas et al., 2022b), and the performance of the used detectors (Weiler et al., 2021; Lux et al., 2024).

In this paper, we concentrate on the ALADIN Fizeau spectrometer channel that is used to measure wind from atmospheric Mie scattering, which mainly originates from aerosols and clouds, leading to narrow-band backscattering signals. Particularly in the last 2 years, significant advances have been made in the detailed understanding of the spectral performance of the Fizeau instrument and the many factors that contribute to its resultant spectral line shape, shift, and width. This understanding has enabled the recent development of two analytic algorithms based on a pseudo-Voigt fitting method and the high-speed four-channel intensity ratio technique R_4, both discussed in Witschas et al. (2023b). These algorithms provide significant advances in both statistical accuracy and valid data gathering compared with the currently available techniques originally developed before launch. Additionally, at a more fundamental level, this detailed understanding permits critical evaluation and review of the many design and experimental parameters of the Fizeau interferometer itself and the overall system.

The paper is thus structured as follows: the basic optical architecture of the Aeolus spectrometers is outlined in Sect. 2, with a summary of the Fizeau design parameters. Significant anomalies of the Fizeau interference pattern, the so-called fringe, found in early tests on ground, could not be explained by classical ray optics and could only be replicated by rigorous wave-optic modelling. Such wave-optic analysis has not previously been applied to Fizeau interferometry and permits rigorous investigation of all aspects of its optical science and performance. For the benefit of readers, this material is presented in a semi-tutorial Appendix with programmatic guidance. Section 3 then describes successive studies of the experimental line shape of Aeolus atmospheric and ground return signals. These proved to be notably different from the simple Lorentzian profiles supposed in the original design and development studies. The observed profiles are well explained by wave-optic modelling, presented in Sect. 4, with detailed consideration of the illumination conditions, including the field of view (FOV) and the angle of incidence (AOI). These results are important for detailed signal-to-noise ratio (SNR) and quantum-limited statistical accuracy. These aspects are summarized in the final section (Sect. 5), together with guidance for future systems of improved performance.

2 The Fizeau spectrometer on Aeolus

2.1 Instrumental design

The instrumental architecture of ALADIN is sketched in Fig. 1. In this paper, attention is directed to the Fizeau interferometer and the optical components that can have an impact on its performance. The setup of the rest of the instrument is only touched upon. A more detailed description of the ALADIN instrument itself is given in ESA (2008) and Reitebuch et al. (2018). The laser transmitters, and their frequency stability, are discussed by Lux et al. (2020, 2021) and the ALADIN spectral performance, and corresponding instrumental drifts are discussed in Witschas et al. (2022b).

ALADIN carried two fully redundant laser transmitters, referred to as flight models A (FM-A) and B (FM-B), emitting laser pulses at a wavelength of 354.8 nm (vacuum) and which are switchable by means of a flip-flop mechanism (FFM). After passing through a beam splitter (BS), a half-wave plate (HWP) used to define the polarization of the laser light, a polarizing beam splitter (PBS) used to separate transmitted and received light, and a quarter-wave plate (QWP) setting the transmitted laser light to circular polarization, the laser beam is expanded and coupled out using a 1.5 m diameter Cassegrain telescope. To monitor the frequency of the outgoing laser pulses and to characterize the frequency-dependent transmission functions of the interferometers, a small portion of the laser radiation that leaks through the beam splitter is further attenuated and used as internal reference signal (Fig. 1, internal reference path). The backscattered radiation from the atmosphere and the ground is collected by the same telescope that is used for emission (monostatic configuration) and is returned to the transmit–receive optics (TRO), where a laser chopper mechanism (LCM) is used to protect the detectors from the signal returned during laser pulse emission, after a narrow-band interference filter (IF) with a width of about 1 nm has
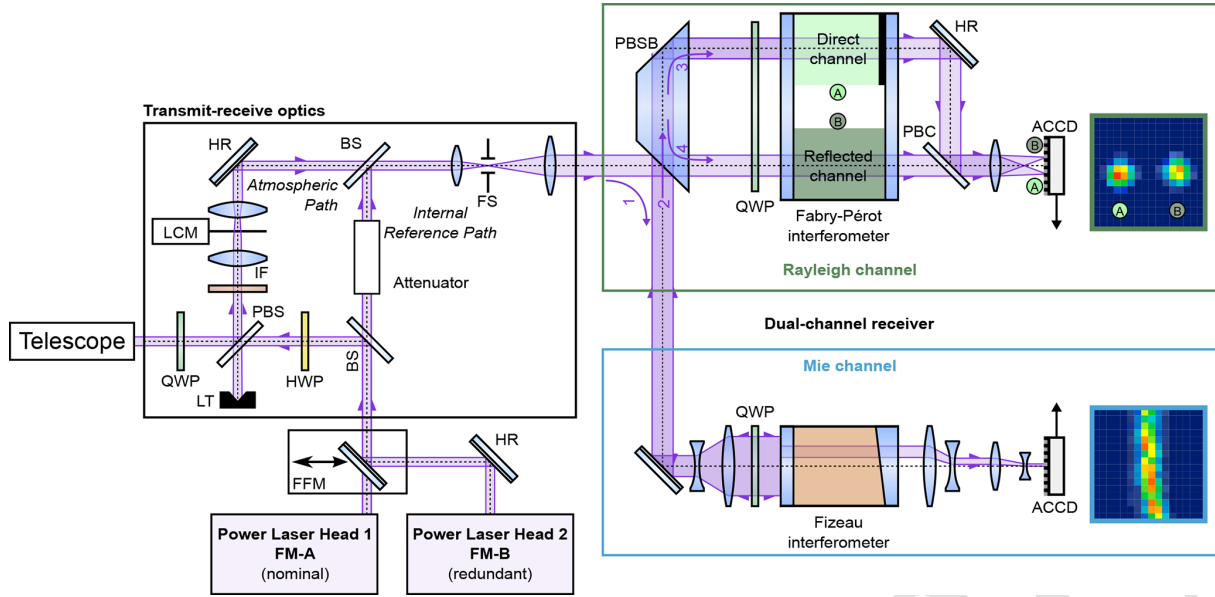
Figure 1. Sketch of the ALADIN optical receiver layout reproduced from Lux et al. (2021). QWP: quarter-wave plate; HWP: half-wave plate; PBS: polarizing beam splitter; PBSB: polarizing beam splitter block; PBC: polarizing beam combiner; FFM: flip-flop mechanism; BS: beam splitter; HR: high-reflectance mirror; LCM: laser chopper mechanism; FS: field stop; IF: interference filter; LT: light trap; ACCD: accumulation charge-coupled device.

blocked the broadband solar background light spectrum. Furthermore, the TRO contains a field stop (FS) with a diameter of 88 μm to set the FOV of the receiver to be only 18 μrad, which is needed to limit the influence of the solar background radiation and the range of angles incident the spectrometers.

Behind the TRO, the light is directed to the interferometers that are used to analyse the Doppler frequency shift of the backscattered light to finally derive the wind speed along the LOS direction of the laser beam. The light is first directed to the so-called Mie channel via a polarizing beam splitter block (PBSB). After increasing its diameter from 20 to 36 mm using a beam expander, which reduces its divergence from 1 mrad to 555 μrad, the light is directed to the Fizeau interferometer, which acts as a narrow-band filter with a full width at half maximum (FWHM) of 58 fm (138 MHz) to analyse the frequency shift of the narrow-band Mie backscatter from aerosol and cloud particles. The Fizeau interferometer spacer is made of Zerodur to benefit from its low thermal expansion coefficient. It is composed of two reflecting plates, separated by 68.5 mm, corresponding to a free spectral range (FSR) of 0.92 fm (2191 MHz), which is chosen to be a fifth of the FSR of the Fabry–Perot interferometers (FPIs) used in the Rayleigh channel. The plates are tilted by 4.77 μrad against each other, and the space in between is evacuated. The resultant interference patterns (fringes) are imaged onto the image zone of an accumulation charge-coupled device (ACCD) detector which has 16×16 pixels (Weiler et al., 2021; Lux et al., 2024). Different laser frequencies interfere at different lateral positions along the tilted plates; therefore the horizontal position of the fringe on the detector is a measure of the frequency of the light incident on the Fizeau. The ACCD does not image the entire spectral range covered by the aperture but only a part of 0.69 fm (1.6 GHz), which is called the useful spectral range (USR). This so-called fringe imaging technique using a Fizeau interferometer (McKay, 2002) was specially developed for ALADIN (ESA, 1999).

The accumulated detector signal is converted into a voltage at the ACCD output and afterwards amplified and digitized. Before digitization, an electronic offset voltage – the so-called detection chain offset (DCO) – is applied to prevent negative values in the signal (Lux et al., 2024).

The light reflected from the Fizeau interferometer is directed towards the so-called Rayleigh channel on the same beam path and linearly polarized in such a direction that the beam is now transmitted through the PBSB. The Rayleigh channel is based on the double-edge technique (Chanin et al., 1989; Flesia and Korb, 1999; Gentry et al., 2000), where the transmission functions of two FPIs are spectrally placed at the points of the steepest slope on either side of the broadband Rayleigh–Brillouin spectrum originating from molecular backscattered light. Further details on the FPI specifications for operation principles are given in Witschas et al. (2022b). For the sake of completeness, the main specifications of the Fizeau interferometer are listed in Table 1.

Table 1. Specifications of the Mie spectrometer of the ALADIN instrument.

Parameter	Value
Material	Zerodur
Aperture	36 mm
Plate spacing	68.5 mm, vacuum gap
Free spectral range	0.92 pm, 2191 MHz
Wedge angle	4.77 µrad
Plate reflectivity (in air)	0.85
Plate reflectivity (in vacuum)	0.88
Useful spectral range	0.69 pm, 1.6 GHz[*]
Fringe FWHM	0.058 pm, 138 MHz[*]
Input divergence	555 µrad full angle[*]

[*] Value taken from Reitebuch et al. (2009).

2.2 Initial findings for the Aeolus Fizeau interferometer from on-ground characterization

In the Fizeau interferometer, light is successively reflected between the surface coatings of the two plates set at the required wedge angle. Multiple interference occurs, ideally leading to straight-line fringes parallel to the wedge vertex. Unlike the FPI, these fringes are localized close to the plate surfaces and are often described as fringes of equal thickness. In the ray-optic approximation the fringes may be considered to trace out the loci of constant path separation between the plates – thus giving straight-line fringes for ideally flat plates. In practice, plates are not perfectly flat; however, minor defects of order $\lambda/100$ across the plates are usually considered to add to the fringe width to a relatively minor and acceptable degree. Detailed analysis of Fizeau fringes has long been carried out by techniques of ray optics, as given for example in the classical text of Born and Wolf (1980) drawing on the analysis of Brossel (1947) and developed by many subsequent authors (Meyer, 1981; Kajava et al., 1993; McKay, 2002).

The plates selected for the ALADIN spectrometer were polished in the early 2000s by the relatively new technique of magneto-rheological finishing (MRF) (Jacobs et al., 1995; Harris, 2011); the impact of this polishing technique on the Fizeau interferometer performance was extensively investigated by Vaughan and Ridley (2013) and Vaughan and Ridley (2016). In the MRF technique, the surface is polished by tracing over the optical element with a comparatively small region of magnetically stiffened cutting medium. For the circular Fizeau plates, the cutting medium was traced in a spiral pattern across the surface. Using the MRF technique, a surface finish/roughness of less than 1 nm is expected. Optical examination and tests confirmed that the overall flatness and smoothness of the plates fell within the specification of better than $\lambda/100$, equivalent to ≈ 4 nm. However, a detailed interferometric examination showed clear evidence of a regular character to the defects with a circular, ring-like structure.

These successive rings/spirals appear to be centred approximately at the centre of the plates. Initial estimates suggested that the pitch, which describes the radial distance between the rings, was ≈ 1 mm with a depth of $\approx \pm 4$ nm. This 1 mm pitch is consistent with the cutting interval of the MRF polishing technique as it spirals over the plate (Vaughan and Ridley, 2016). In contrast, classical polishing techniques are different. Here, defects of $\lambda/100$ might be expected but spread in a single cycle across the full area of the plates to give a weak departure from flatness – often described as "dishing" or "bowing". In the MRF technique, however, the plate surface is much more rapidly corrugated with a peak-to-valley distance for the defects of order 0.5 mm, which corresponds to half of the pitch.

Initial examination in the laboratory of the Fizeau fringes revealed two rather unusual findings (Francou et al., 2017). First, the fringes, rather than being generally uniform and approximately straight lines, were strongly modulated and appeared to be broken up along their length into regions of high and low intensity. Second, as the input frequency was varied, meaning the fringe moved laterally across the plates, these regions of high and low intensity traced out what appeared to be equispaced circular rings with a centre close to the centre of the plates. It thus became imperative to examine the potential impact of these findings on the spectroscopic performance of the Fizeau interferometer. The immediate concern was the potential distortion of the vertically integrated fringe profiles and resultant frequency shifts, which could lead to significant errors in the frequency measurement and the wind velocity accuracy. It was rapidly established that classical techniques of ray-optic analysis, which do not account for diffraction and changes of local slope at the plate defects, could not explain the observed fringe anomalies. Accordingly, a novel wave-optic technique (see e.g. Jakeman and Ridley, 2006) was introduced and shown to accurately reproduce the observed fringes. The development of these methods and extension to the optical science and performance of Fizeau interferometers is detailed in the Appendix and provides an underlying framework for the following sections.

3 Examination and analysis of Aeolus Fizeau fringes

From the most basic consideration of the Aeolus Fizeau interferometer, the form of the raw signal fringe profile $\mathcal{P}_{\mathrm{Raw}}$, as it emerges from the detector, may be derived from

$$\mathcal{P}_{\mathrm{Raw}} = \mathcal{P}_{\mathrm{Las}} * \mathcal{P}_{\mathrm{Fiz}} * \mathcal{P}_{\mathrm{Det}}, \tag{1}$$

where $*$ denotes the convolution by the folding integral, $\mathcal{P}_{\mathrm{Las}}$ the laser pulse profile, $\mathcal{P}_{\mathrm{Fiz}}$ the Fizeau instrument profile, and $\mathcal{P}_{\mathrm{Det}}$ the detector channel spectral profile. Equation (1) gives a continuous profile. The actual discrete detector outputs can be found by evaluating it at locations corresponding to the centres of the detector pixels. Note, also, that if the frequency of the input laser light is varied in small steps, values

of $\mathcal{P}_{\text{Raw}}$ can be found at sub-pixel intervals (see e.g. Marksteiner et al., 2018, 2023).

The ALADIN laser transmitters were developed and built by the company Selex Galileo (today Leonardo), who characterized $\mathcal{P}_{\text{Las}}$ by early laboratory measurements to be smaller than 50 MHz (FWHM) with a supposed Lorentzian spectral shape (Cosentino et al., 2012, 2017). The Fizeau interferometer was manufactured by the company Thales SESO (Francou et al., 2017). Its design specifications, notably plate reflectivity and wedge angle, were selected to minimize the inherent asymmetry of the Fizeau fringes (see also Sect. 2). It was thus considered that the basic instrumental profile for monochromatic input would be close to the Airy form (see also Eq. 8), which can be conveniently written as a sum of successive Lorentzians, spaced by the free spectral range Γ_{FSR}. With the specification of $\Gamma_{\text{FSR}} = 2191$ MHz and a plate reflectivity $R = 0.88$ (in vacuum), the equivalent single Lorentzian profile representing $\mathcal{P}_{\text{Fiz}}$ would have a width of $\Gamma_{\text{FSR}} \cdot (1-R)/(\pi\, R^{1/2}) \approx 90$ MHz. Further, with the selected fringe imaging lens, the 16 detector channels closely approximate a rectangular "top-hat" function $\mathcal{P}_{\text{Det}}$ with a width of ≈ 100 MHz. On this analysis, with $\mathcal{P}_{\text{Las}}$ and $\mathcal{P}_{\text{Fiz}}$ both having a Lorentzian spectral shape, their combined profile would also be Lorentzian with a width given by their linear sum equal to ≈ 140 MHz. The folding integral of a Lorentzian and a top-hat function has a width given by the root sum of squares, which leads to a resultant FWHM for the full raw profile $\mathcal{P}_{\text{Raw}}$ of ≈ 172 MHz. These considerations have provided the basis for the original analytical algorithm, which was developed for the analysis of Aeolus fringes and which has been refined through successive improvements and upgrades (Reitebuch et al., 2018). In essence, it applies a best-fitting procedure of a pixelated Lorentzian to the measured fringes after the signal has been corrected for the DCO and the solar background signal.

In summary, the foregoing parameters immediately indicate the problems of reliable, unbiased analysis. The actual observed channel contents from the detector are highly averaged representations (resolution of ≈ 100 MHz) of the incident fringe profile (width of ≈ 140 MHz). Inevitably, any fine detail is irretrievably lost, and any analytic technique for derivation of frequency shift and width will have some bias and inaccuracies depending on the assumed model of the fringe profile and how closely representative it is of the true fringe. These errors are likely to be reduced for model profiles that most accurately match the actual profile. This provides an additional underlying rationale for the present investigations.

3.1 Further contribution to the Fizeau fringe profile

Several other factors can make a greater or lesser contribution to the Fizeau interferometer output profile $\mathcal{P}_{\text{Raw}}$ and need to be considered. A partial listing would include, for example, the spectral character of the incoming light field, such as spurious background and laser frequency instability and jitter. Other important considerations are the physical characteristics of the incoming beam including AOI, FOV, and speckle effects; the non-uniform illumination of the Fizeau plates; and the impact of plate defects. Additionally, residual asymmetries in the interferometric Fizeau profile may require correction, while detector performance issues – such as pixel width non-uniformity, quantum efficiency variations, edge effects, spill-over, and charge transfer efficiency – can also impact results. These factors are discussed in greater detail in the following sections where relevant. However, one factor has an overall influence on $\mathcal{P}_{\text{Raw}}$, namely the non-uniformity of plate illumination. Unlike FPI fringes, the Fizeau fringe is localized in the plane of the Fizeau plates, which must then be focused onto the detector plane. Thus, the precise form of the Fizeau fringe registered by the detector is strongly impacted by any lack of uniformity of the incident illumination at the plates. The Aeolus internal reference beam is well established as non-uniform (see e.g. Witschas et al., 2022b) and, without considerable post-detection correction, leads to distorted fringes (Francou et al., 2017).

In comparison, Aeolus ground and atmospheric returns should provide uniform illumination at the entrance to the telescope, but this is, of course, subject to obscuration within the telescope optics, most notably the secondary mirror and its support structures. Various early analyses based on simple geometrical considerations of the obscuration were attempted but are now superseded by the more soundly based EMSR (effective Mie spectral response) correction (Wang et al., 2024; Reitebuch et al., 2024). In this derivation, it is considered that the broadband background signal, following a Rayleigh–Brillouin (RB) spectral distribution (Witschas et al., 2010; Witschas, 2011a, b), is close to spectrally uniform (i.e. flat) across the Fizeau spectral range. Hence, by averaging and comparing Fizeau channel contents from areas dominated by pure RB signals, a good characterization of the obscuration in the Fizeau telescope optics was derived and used for correction. Subsequent wave-optic modelling of the overlap of orders for the RB spectrum established that the background across 1 order was indeed completely flat (see also Sect. 4.5). It is worth mentioning that the EMSR corrects not only for the obscuration but also for the actual illumination of the Fizeau interferometer and its temporal evolution. The EMSR correction thus provides the possibility of retrieving the Fizeau fringe spectral shape with high accuracy. This is particularly important for strong ground returns which should be essentially monochromatic with no additional Mie or Rayleigh response. Based on this, fringes from ground return signals were acquired during instrument response calibration (IRC) measurements. An IRC is performed with the instrument LOS pointing in nadir direction and changing the laser frequency in steps of 25 MHz over a spectral range of 1000 MHz (Marksteiner et al., 2018, 2023). The resulting ground return signals of such IRC measurements enabled the construction of prototype Fizeau fringes

and the detailed analysis of their spectral characteristics, as is discussed in the following sections.

3.2 Fizeau fringe characterization by non-linear fit procedures

To analyse the spectral characteristics of the Aeolus Fizeau fringes in detail, internal reference signals (INT) as well as atmospheric and ground return signals (ATM) from an IRC measurement performed on 4 July 2019 are used as shown in Fig. 2. To avoid the influence of broadband RB background in the ATM signal, only the four fringes with the highest signal intensities were chosen and averaged as shown by the black circles in Fig. 2b. Panel (a) shows the corresponding fringe from the INT signal, which was also EMSR-corrected using the illumination function as it is for instance characterized by instrument spectral registration (ISR) measurements (Witschas et al., 2022b). As the illumination characteristics are different for the ATM and the INT path, different EMSR corrections have to be applied. Furthermore, both signals are corrected for the DCO, and the ATM signal is additionally corrected for the solar background signal.

As described above, the Fizeau instrument function $\mathcal{P}_{\text{Fiz}}$ as well as the laser profile $\mathcal{P}_{\text{Las}}$ can be approximated by a Lorentzian peak function according to Born and Wolf (1980), Vaughan (1989), and Witschas et al. (2023b):

$$\mathcal{L}(x) = \frac{2\mathcal{I}_{\mathcal{L}}}{\pi} \cdot \frac{\Gamma_{\mathcal{L}}}{4(x - x_0)^2 + \Gamma_{\mathcal{L}}^2}, \tag{2}$$

where $\mathcal{I}_{\mathcal{L}}$ denotes the area under the peak, $\Gamma_{\mathcal{L}}$ the FWHM, and x_0 the centre position. The raw fringe profile, as given by Eq. (1), has additionally been convolved with the detector profile $\mathcal{P}_{\text{Det}}$, which can be described by a top-hat function according to

$$\mathcal{P}_{\text{Det}} = \frac{1}{\Gamma_{\text{TH}}} \cdot H(x) \cdot \left(\frac{1}{4} - \left(\frac{x}{\Gamma_{\text{TH}}} \right)^2 \right), \tag{3}$$

where $H(x)$ is the Heaviside step function, and Γ_{TH} denotes the width of the top hat. The convolution of Eqs. (2) and (3) can be derived analytically and results in a pixelated Lorentzian $\mathcal{L}_{\text{px}}(x)$ according to

$$\mathcal{L}_{\text{px}}(x) = \frac{\mathcal{I}_{\mathcal{L}_{\text{px}}}}{\pi \cdot \Gamma_{\text{TH}}} \cdot \left(\arctan\left(\frac{-2x_0 + \Gamma_{\text{TH}} + 2x}{\Gamma_{\mathcal{L}}} \right) \right. $$
$$\left. + \arctan\left(\frac{2x_0 + \Gamma_{\text{TH}} - 2x}{\Gamma_{\mathcal{L}}} \right) \right), \tag{4}$$

where $\mathcal{I}_{\mathcal{L}_{\text{px}}}$ denotes the area under the peak. Now, Eq. (4) is applied in a least-square fit procedure to the measured prototype fringes, as shown by the dashed blue lines in Fig. 2. The resulting fit parameters are given in the inset. It is obvious that the accordance of the fit with the measured fringe is not good, especially in the wings of the fringe, and this is most pronounced for the ATM fringe (Fig. 2b). The resulting

widths are $\approx 160\,\text{MHz}$ for the INT and $\approx 185\,\text{MHz}$ for the ATM signal, which is close to the estimate of $\approx 172\,\text{MHz}$ as given above, when considering a laser pulse profile of width $\approx 50\,\text{MHz}$ and a Fizeau profile of width $\approx 90\,\text{MHz}$, both having a Lorentzian shape. However, the poor accordance of the fit reveals that the actual contributions to the fringe profile are of different nature.

In light of this, it was investigated if a Voigt function $\mathcal{V}(x)$, defined as the convolution of a Lorentzian $\mathcal{L}(x)$ (Eq. 2) and a Gaussian peak profile $\mathcal{G}(x)$, represents the prototype fringe with better accuracy:

$$\mathcal{V}(x) = (\mathcal{L} * \mathcal{G})(x), \tag{5}$$

where $*$ denotes the convolution of the folding integral, and

$$\mathcal{G}(x) = \left(\sqrt{\frac{4\ln 2}{\pi}} \cdot \frac{1}{\Gamma_{\mathcal{G}}} \right) \cdot \exp\left(-4\ln 2 \cdot \left(\frac{x - x_0}{\Gamma_{\mathcal{G}}} \right)^2 \right), \tag{6}$$

with $\Gamma_{\mathcal{G}}$ being the FWHM.

Although the Voigt function cannot be represented in an analytically closed form, or rather without using special functions, its FWHM $\Gamma_{\mathcal{V}}$ can be approximated with an accuracy of better than $0.02\,\%$ according to Olivero and Longbothum (1977) by

$$\Gamma_{\mathcal{V}} = 0.5346\,\Gamma_{\mathcal{L}} + \sqrt{0.2166\Gamma_{\mathcal{L}}^2 + \Gamma_{\mathcal{G}}^2}. \tag{7}$$

Equation (5) is used to perform a numerical least-square fit to the prototype fringes as shown by the purple lines in Fig. 2. The resulting fit parameters are given in the inset. It is obvious that there is excellent accordance between the prototype fringes and the fit for both the INT and the ATM signals. Both the slopes and the wing intensity are reproduced very well. The fit yields an FWHM $\Gamma_{\mathcal{V}}$ of $(1.69 \pm 0.02)\,\text{px}$ or $(169 \pm 2)\,\text{MHz}$ for the INT and $\Gamma_{\mathcal{V}} = (2.10 \pm 0.01)\,\text{px}$ or $(210 \pm 1)\,\text{MHz}$ for the ATM signal. For the INT signal, $\Gamma_{\mathcal{L}} = (0.86 \pm 0.05)\,\text{px}$ and $\Gamma_{\mathcal{G}} = (1.17 \pm 0.05)\,\text{px}$ and for the ATM signal $\Gamma_{\mathcal{L}} = (0.72 \pm 0.06)\,\text{px}$ and $\Gamma_{\mathcal{G}} = (1.68 \pm 0.04)\,\text{px}$. From this, interesting characteristics of the fringes can be derived. First, it can be seen that the width of the INT fringe ($169\,\text{MHz}$) is close to expectations; however, the ATM fringe is significantly broader ($210\,\text{MHz}$). Furthermore, it can be realized that a large Gaussian component has to be considered in order to describe the prototype fringes with sufficient accuracy, which is in contrast to all original expectations. Wave-optic analyses, as later discussed in Sect. 4.2, have revealed, that, for the ATM path, an off-axis illumination of the Fizeau interferometer of $\approx 400\,\mu\text{rad}$ with a divergent laser beam ($\approx 500\,\mu\text{rad}$) can explain the observed Voigt-shape and width of the Aeolus Mie fringes.

The foregoing discussions outline the complexities of Fizeau fringe formation and raise questions about how to usefully resolve them. In order to answer these questions, the underlying components $\mathcal{P}_{\text{Las}}$ and $\mathcal{P}_{\text{Fiz}}$ and the impact of $\mathcal{P}_{\text{Det}}$
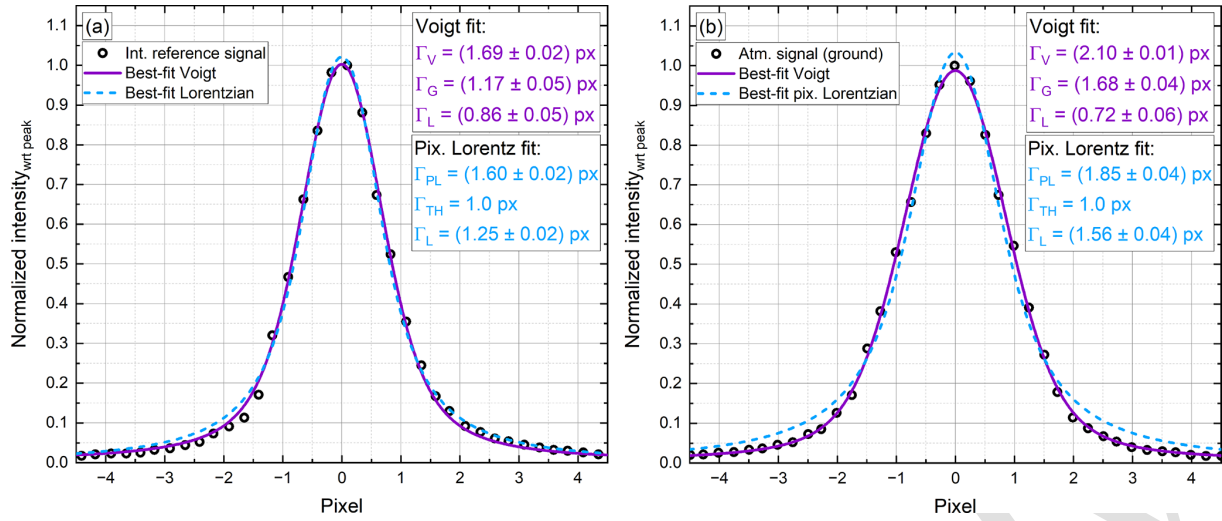
Figure 2. Averaged Aeolus Fizeau fringes (EMSR-corrected and background-signal-corrected) depicted by the black circles for the internal reference signal **(a)** and the ground return signal **(b)**, retrieved from the instrument response calibration (IRC) measurement performed on 4 July 2019. The blue line indicates a best fit of a pixelated Lorentzian according to Eq. (4), and the purple line indicates a best fit of a Voigt profile according to Eq. (5). Details of the fit results are given in the inset. See text for explanation of the symbols.

are examined in Sect. 3.3, leading to a better understanding of the physical/optical nature and the implications for future design.

3.3 Calculation of the basic components of the Aeolus Fizeau interferometer fringe

In the framework of a pre-development programme that was conducted in the early phase of the Aeolus preparation (Durand et al., 2004), laboratory tests of the receiver breadboard were performed, including the characterization of the Fizeau interferometer. These measurements also defined the Fizeau parameters as summarized in Table 1.

Initial laboratory measurements in air suggested experimental line widths of 105 MHz, in reasonable agreement with a reflectivity finesse of $N_R = 20.8$ and consistent with a plate reflectivity of $R \approx 0.85$. However, in later measurements in vacuum, line widths somewhat less than 100 MHz were observed. As shown by Stolz et al. (1993), reflectivity changes of $\approx 3\%$ to shorter wavelengths can appear when going from air to vacuum, due to changes in the dielectric coating layers. Reflectivity versus wavelength curves for a pair of plates were available and showed that the reflectivity in vacuum, for such a 3 % wavelength shift, was closer to 0.88. This latter value has accordingly been used as a good representative value for further investigations discussed in this study.

Furthermore, the Fizeau plates received a detailed examination of surface characteristics, revealing not only the semi-regular fine-scale defects due to MRF finishing but also structures across a larger scale. Wave-optic modelling for these measured defects showed fluctuations of frequency response across the plate in the range of −10 to 2 MHz, compared with

the input frequency (Vaughan and Ridley, 2013; Vaughan and Ridley, 2016). The apparent FWHM also varied over 105 ± 7 MHz. Later examination of the fringe profile shapes indicated a Gaussian component that could approach up to 20 MHz induced by the aforementioned plate defects.

Before the mission, the spectral pixel width was characterized in different laboratory tests to be in the range of 95 to 105 MHz. Some of this variation was attributed to uncertainties in the precise optical magnification between the detector plane and the Fizeau instrument. Precise investigations of the Aeolus system based on regular IRC measurements (Marksteiner et al., 2023) support a spectral pixel width of 94 to 95 MHz throughout the entire mission time. For the sake of simplicity and without impacting the drawn conclusions, a spectral pixel width of 100 MHz is used throughout this study.

The uncertainties of the fringe position and the spectral profile of these findings are relatively small, of order 10 MHz or less. As such, they are unlikely to explain the considerably larger magnitude of the ATM prototype fringe FWHM of 2.10 px (≈ 210 MHz), as discussed in Sect. 3.2. This would in fact require an input Lorentzian of ≈ 182 MHz, to be folded with the top hat of 100 MHz (1 px). And even then, the overall fringe profile cannot be described accordingly as shown in Fig. 2.

The following three subsections describe techniques that attempt to analyse the prototype fringe and to quantify the profiles and magnitude of the individual contributions (laser, Fizeau, detector). These techniques rely on the evaluation and comparison of the pixel contents across the prototype fringe, namely from the total energy within the fringe (Sect. 3.3.1), from the relative pixel content around

the fringe peak (Sect. 3.3.2), and from consideration of the pixel content in the outer region of the fringe (Sect. 3.3.3). It may be noted that, for a large detector function with a width comparable to the one of the input fringe, distortion of the output fringe is large. Commonly applied ratio techniques, using profile widths at different relative intensities, proved liable to error and unpromising. Hence the preference for examination of channel content is detailed below.

3.3.1 Calculation of fringe components from total fringe content

From the prototype fringe as shown in Fig. 2, the total content $\mathcal{I}_{\text{fringe}}$ is numerically determined to be $\mathcal{I}_{\text{fringe}} = 2.505$, where the fringe has a peak normalized at unit intensity ($\mathcal{I}_{\text{peak}} = 1$). The corresponding FWHM is determined by a best fit of Eq. (5) to the data (Fig. 2a, purple line) and using Eq. (7), resulting in $\Gamma_{\mathcal{V}} = 2.10\,\text{px}$. In order to quantify the respective Lorentzian and Gaussian contribution to the Voigt-shaped profile from these values, the Voigt profile table provided by Tudor Davies and Vaughan (1963) is used. This table characterizes the Voigt profile regarding intensity and width for various Lorentzian-to-Gaussian ratios. Hence, using the respective values from the prototype fringe as mentioned above, the Lorentzian and Gaussian contribution can be read from this table. For instance, the total fringe content is expressed as $\mathcal{I}_{\text{fringe}} = p \cdot \mathcal{I}_{\text{peak}} \cdot \Gamma_{\mathcal{V}}$, where p is a numerical value for any specific Voigt function.

From the parameters retrieved for the prototype fringe, the value of $p = 2.505/(1 \cdot 2.10) = 1.19$. Referring to the Voigt tables, the corresponding fractional values of the components can be read to be $\mathcal{L}_{\text{fraction}} = 0.30$ and $\mathcal{G}_{\text{fraction}} = 0.83$. Given a FWHM of 2.10 px, the corresponding components are $L_{\text{FWHM}} = 0.63\,\text{px}$ and $G_{\text{FWHM}} = 1.74\,\text{px}$. With $1\,\text{px} \approx 100\,\text{MHz}$, this initial estimate of $L_{\text{FWHM}} \approx 63\,\text{MHz}$ appears slightly smaller than anticipated, while the G component is somewhat larger. However, this outcome is reasonable as the procedure essentially "force-fits" the prototype fringe using a Voigt profile composed solely of pure L and G components. The pixelated detection introduces the large extra component of a top hat (1 px wide). Effectively, this top hat may be considered to operate as a "super Gaussian" with zero wings. When folded with other functions, notably L and G, the top hat serves to reduce the apparent L component, and enlarge the G component, in the subsequent force fit to a pure Voigt function. It is in fact possible to introduce first-order corrections to the above calculation, taking account of the relative changes of peak height and width due to folding with a top-hat function. With these corrections, the components are given by $L_{\text{FWHM}} \approx 0.85\,\text{px}$ and $G_{\text{FWHM}} \approx 1.47\,\text{px}$.

In summary, this straightforward procedure provides strong evidence that the fringe output from the Fizeau instrument has a large Gaussian component of about 147 MHz. Most notably the Lorentzian component of about 85 MHz ap-
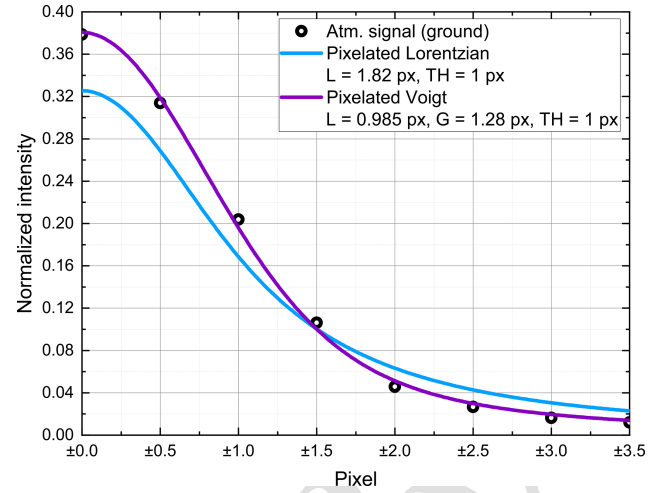
Figure 3. Plots of fractional fringe content for the pixels around the peak for the experimental prototype fringe built up from Aeolus ground returns (black circles) (see also Fig. 2b), compared with a pixelated Lorentzian according to Eq. (4), with $\Gamma_{\mathcal{L}} = 1.82\,\text{px}$ and $\Gamma_{\text{TH}} = 1\,\text{px}$ (light-blue line), and with a pixelated Voigt function, with $\Gamma_{\mathcal{L}} = 0.985\,\text{px}$, $\Gamma_{\mathcal{G}} = 1.28\,\text{px}$, and $\Gamma_{\text{TH}} = 1\,\text{px}$ (purple line).

pears to be close to that calculated for the finesse-limited line width of the Fizeau interferometer itself ($\approx 90\,\text{MHz}$).

3.3.2 Calculation of components from individual channel contents close to the peak

In a next step, the individual channel contents in the prototype fringe are examined in terms of their fractional content compared with the content of the full fringe (i.e. the 22 channels of a full FSR). From the prototype records, the content of the individual channels is calculated as a fraction of the total content across the complete fringe. This summation requires that the fringe is considered across the full FSR (closely equivalent to 22 channels, corresponding to $\Gamma_{\text{FSR}} = 2191\,\text{MHz}$) as compared with the 16 channels of the detector (USR). Simple estimations of the content in these six outer channels amount to $\approx 1.9\,\%$ of the complete profile. The resultant corrections across the channel contents close to the peak are less than 0.01 (fractional unit). The fractional single channel contents, as averaged for the two symmetric, nominally equal channels on either side of the centre, are plotted in Fig. 3.

As a first comparison, the pixelated Lorentzian input fringe with $\Gamma_{\mathcal{L}} = 1.82\,\text{px}$, convolved with a top-hat function of $\Gamma_{\text{TH}} = 1\,\text{px}$ width, is considered (light-blue line) according to Eq. (4), resulting in a total width of $\approx 2.1\,\text{px}$. For this pixelated Lorentzian, although the width is equal to the one determined for the experimental prototype fringe (black circles), the calculated fractional contents are obviously different. Most notably, the two central pixels of the prototype fringe are about 0.05 (fractional unit) greater. Correspond-

ingly, the two outer pixels are more than 0.015 smaller. The second comparison (purple line) is based on a Voigt function, with $\Gamma_{\mathcal{L}} = 0.985$ px and $\Gamma_{\mathcal{G}} = 1.28$ px, giving a FWHM of $\Gamma_{\mathcal{V}} = 1.89$ px (Eq. 7), numerically folded with a top-hat function of width $\Gamma_{\mathrm{TH}} = 1$ px, to result in a total width of 2.1 px. The close correspondence of this profile with the prototype fringe values provides further strong confirmatory evidence that the Fizeau fringe before detection is made up of a Lorentzian of about 1 px (100 MHz) and a Gaussian of about 1.3 px (130 MHz).

3.3.3 Analysis of the outer part of the fringe

For a detailed analysis of the outer part of the prototype fringe, the Lorentzian formula (Eq. 2) is no longer a good approximation, and the Fizeau fringe is better described by the classical Airy formulation according to (see e.g. Hernandez, 1986; Vaughan, 1989)

$$I_T = I_0 \cdot \frac{T^2}{(1-R)^2} \cdot \frac{1}{1 + F\sin^2(\varphi/2)}, \qquad (8)$$

where $F = 4R/(1-R)^2$ is the finesse coefficient, R and T the plate reflectivity and transmission terms, and φ the phase lag per optical transit of the plate separation. Note the difference to the commonly used reflectivity finesse, which is given by $N_{\mathrm{R}} = (\pi/2) \cdot F^{1/2} = \pi R^{1/2}/(1-R)$. The Airy function $\mathcal{A}(\varphi)$ is accordingly given by $\mathcal{A}(\varphi) = \left[1 + F\sin^2(\varphi/2)\right]^{-1}$, with typical values of $N_{\mathrm{R}} \approx 24.6$ and $F \approx 244$, for a mean plate reflectivity of $R \approx 0.88$. In the outer part of the fringe, i.e. $\varphi/2 \gtrsim \pi/3$, $A(\varphi)$ can be closely approximated by $F^{-1}\left[\sin^2(\varphi/2)\right]^{-1}$. As discussed by means of Eq. (1), the detector raw signal is additionally impacted by the laser pulse profile (e.g. a Gaussian) and the detector channel spectral width (e.g. a top hat). The impact of these contributions on the outer part of the fringe profile is illustrated in Fig. 4, which shows the fringe development of a basic Airy profile of unit height and FWHM of 1 px (black), convolved with a Gaussian function of width 1.2 px (magenta) and further broadened by the top-hat detector function of width 1.0 px (light blue). All three curves are normalized to unit area.

It can be readily observed that the convolution of the Gaussian and the top hat results in negligible changes in the outer part of the fringe. This is due to the fact that the Gaussian and top-hat functions do not have extended wings that would redistribute energy into the outer regions.

In a next step, the Airy profile $\mathcal{A}(\varphi)$ is compared to the outer part of the ATM prototype fringe. From the prototype fringe data, F^{-1} is determined to be $(4.22 \pm 0.20) \times 10^{-3}$, which equates to $F = 237 \pm 11$ and $N_{\mathrm{R}} = 24.2 \pm 0.6$. The corresponding Airy profile (light-blue line) and the ATM prototype fringe data (black circles) are plotted in Fig. 5.

The reflectivity finesse $N_{\mathrm{R}} = 24.2$ would suggest that the basic Airy function has a width of 0.91 px, and the associ-
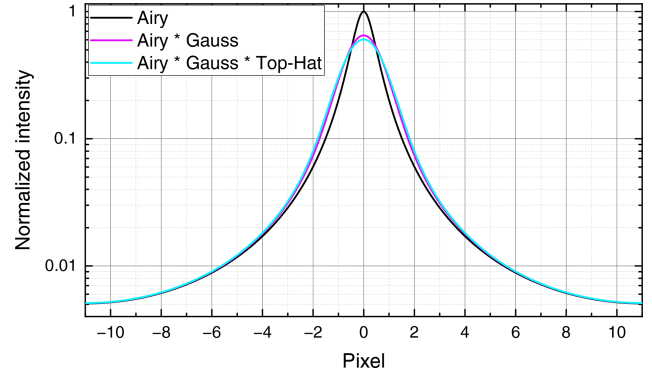
Figure 4. Basic Fizeau Airy type fringe (black) convolved with a Gaussian function of width 1.2 px (magenta) and the top-hat detector function of width 1.0 px (light blue). The total energy (i.e. the area) is conserved. The y axis is in log scale.
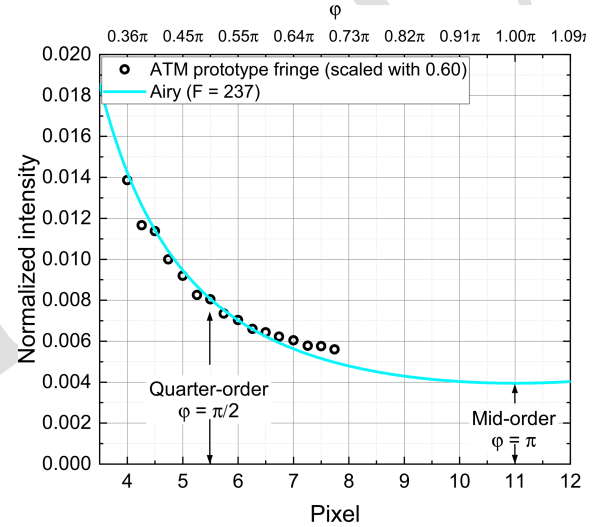
Figure 5. Airy fringe according to Eq. (8) over pixels 4 to 11 ($\varphi > 0.35\pi$) for $F = 237$ (light-blue line). The 16 values (black dots) of the ATM prototype fringe (see also Fig. 2b) were averaged to give a best representative fit for F.

ated Gaussian width would be ≈ 1.3 px to make up the output fringe from the Fizeau, which is then detected as the prototype fringe. It would, of course, be possible to repeat this evaluation in an iterative procedure, with the new starting point of an Airy profile of width 0.91 px. However, it does not appear particularly worthwhile. All evidence indicates that the observed fringe initially exhibits a comparatively narrow Airy-type profile, close to Lorentzian form, with a width slightly less than 1 px (100 MHz). This profile is then broadened by successive physical processes that approximate Gaussian and top-hat functional forms.

In summary, the various investigations across the prototype fringe clearly establish that the output fringe from the Fizeau is close to a Voigt function, with a large Gaussian

component of about 1.3 px. So, the obvious questions are as
follows: what are the physical mechanisms which have led
to this unexpected result, and what lessons can be drawn for
system performance and improvement?

The outcome of this study further triggered the update
of the Aeolus processor, which was still using a pixelated
Lorentzian fit to derive the Fizeau fringe positions and the
corresponding wind speeds by means of the Mie-core 2 al-
gorithm (Reitebuch et al., 2014). As the Voigt function has
no simple analytical solution without special functions, the
new Mie-core 3 algorithm will be based on the pseudo-Voigt
approximation, which is a linear combination of $\mathcal{L}(x)$ and
$\mathcal{G}(x)$, with identical widths ($\Gamma_{\mathcal{L}} = \Gamma_{\mathcal{G}}$). Based on Aeolus
Airborne Demonstrator data, which have similar character-
istics to Aeolus data, Witschas et al. (2023b) demonstrated
the much better performance of the pseudo-Voigt fit com-
pared to the Lorentzian fit. In particular, 50 % more data
points could be reached while keeping the resulting random
errors equally sized. In addition, a novel algorithm (R$_4$) has
been developed by Witschas et al. (2023b), which is based
on a ratio constructed from the four central pixel channels
around the fringe peak. After calibration, the R$_4$ algorithm is
demonstrated to provide similar quality as the pseudo-Voigt-
fit-based algorithm but with a computation time that is faster
by 2 orders of magnitude.

4   Modelling and analysis of contributory factors to the Fizeau fringe profile

The previous section has established that the Aeolus Fizeau
fringe, prior to detection, is primarily made up of a
Lorentzian component of $\approx 100\,\text{MHz}$ ($\approx 1.0\,\text{px}$) FWHM,
folded with a Gaussian component up to $\approx 130\,\text{MHz}$
($\approx 1.3\,\text{px}$) FWHM. This present section investigates the
physical/optical basis of these terms and particularly the
somewhat unexpected magnitude of the Gaussian compo-
nent.

4.1   The laser pulse profile

The pulse duration $\Delta\tau$ of Aeolus laser pulses was char-
acterized to be $\Delta\tau \approx 20\,\text{ns}$ (Lux et al., 2021; Cosentino
et al., 2012). Depending on the actual pulse spectral shape,
this corresponds to a Fourier-transform limit of the pulse
spectral width (FWHM) of $\Delta\nu \geq 0.441/\Delta\tau \approx 22\,\text{MHz}$
for a Gaussian-shaped laser pulse and $\Delta\nu \geq 0.142/\Delta\tau$
$\approx 7.1\,\text{MHz}$ for a Lorentzian-shaped laser pulse (Koechner,
2013). However, heterodyne measurements of the ALADIN
Airborne Demonstrator laser transmitter, which is based on
a similar configuration with comparable specifications, re-
vealed that the actual line width was approximately twice
the Fourier-transform limit (Schröder et al., 2007). This spec-
tral broadening is attributed to a frequency chirp, most likely
caused by changes in population inversion during pulse evo-

lution. As the same effect is assumed for the Aeolus lasers,
the spectral width is expected to be larger than the Fourier-
transform limit.

A careful analysis of the intensity spectrum published by
Schröder et al. (2007) by width ratio techniques and tables
of Voigt integrals revealed a spectral width of 15.6 MHz (for
the infrared beam at 1064 nm), dominated by a large Gaus-
sian component of $(14.7 \pm 0.5)\,\text{MHz}$, folded with a much
smaller Lorentzian component of $(1.7 \pm 0.9)\,\text{MHz}$. These are
derived from the fractional components $\mathcal{G}_{\text{fracction}} = 0.94 \pm 0.3$
and $\mathcal{L}_{\text{fraction}} = 0.11 \pm 0.6$, where the errors are indicative
"limit" errors from the ratios. The measurement of such small
Lorentzian fractions is towards the limit of available accu-
racy.

In conclusion, on frequency tripling from 1064 nm to the
operational Aeolus wavelength at 355 nm, one would thus ex-
pect the laser pulse profile to be dominated by a Gaussian
component of $\approx 45\,\text{MHz}$ FWHM, with a Lorentzian compo-
nent of less than $\approx 5\,\text{MHz}$.

4.2   Wave-optic modelling of FOV and AOI

In the period prior to launch, extensive wave-optic modelling
of speckle-type signals and their equivalent optical FOV was
carried out (Vaughan and Ridley, 2013; Vaughan and Ri-
dley, 2016). This work largely concentrated on small AOI
and questions of apparent frequency shift relative to the in-
put frequency. For single speckle patterns, so-called "frozen
speckle", shifts of a few tens of megahertz (MHz) were ev-
ident. With appropriate temporal and spatial averaging of
speckle, as would be expected for most practical operations,
these fringe shifts are reduced by the square root of the num-
ber of independent speckle patterns, with small increases in
fringe width. These values, evaluated for small AOIs, were
thus considered within acceptable bounds.

After launch, evidence steadily accumulated that op-
erational AOIs were indeed considerably larger. For the
ALADIN FPIs, AOIs greater than $400\,\mu\text{rad}$ were required
to explain the measured fringe widths and shifts, as exten-
sively discussed by Witschas et al. (2022b), particularly in
their Sect. 6. This prompted extensive modelling of Fizeau
fringes at such larger AOI. Successive steps in this procedure
are illustrated in the following diagrams.

Figure 6a shows fringe profiles for plane-wave illumina-
tion with the nominal Aeolus fringe parameters as given
in Table 1. At normal incidence (AOI $= 0\,\mu\text{rad}$), the re-
sultant fringe is reasonably symmetric (black line). How-
ever, at AOI $= 300\,\mu\text{rad}$, the fringe is considerably broad-
ened and distorted with a small distinct secondary maxi-
mum at the side (purple line). Here, the AOI is defined to
be positive when the incoming radiation is tilted towards the
apex of the Fizeau wedge. Note that the bottom x axis is
given in millimetres, and the top x axis indicates the cor-
responding frequency considering the conversion factor of
$59.2\,\text{MHz}\,\text{mm}^{-1}$, as used in the wave-optic model.
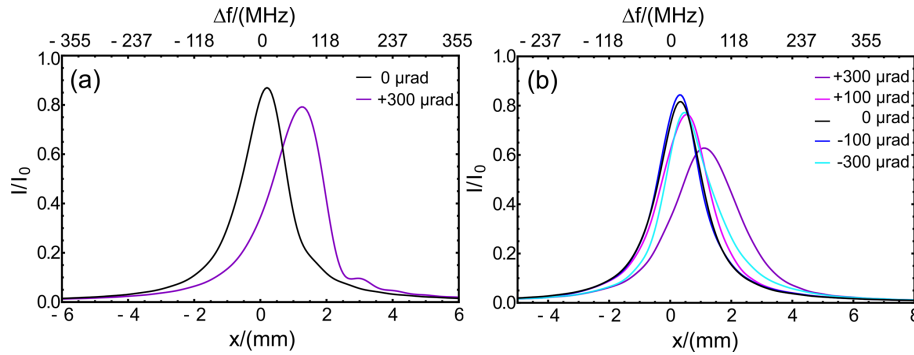
Figure 6. Modelled fringe profiles for Aeolus Fizeau nominal parameters, as given in Table 1. **(a)** Plane wave illumination at nominal incidence (black line) and with AOI = 300 µrad (purple line). **(b)** Illumination with FOV = 500 µrad at different AOI values, as given in the inset.

The adjacent Fig. 6b, for a cone angle illumination FOV = 500 µrad, used as an approximation of the actual FOV of 555 µrad (see also Table 1), shows model fringes for AOIs up to ±300 µrad in x tilt, with y tilt = 0. These have been calculated in a physically realistic way, by starting with an input field consisting of randomly phased components with a specified angular distribution, i.e. a speckle pattern. Averaging of many uncorrelated fringe intensity patterns mimics temporal integration and produces the final fringe profile. A number of 100 averages in total are typically sufficient for a fringe spatially integrated along its vertical axis, i.e. the y direction. Here, we are assuming a Gaussian-profiled FOV, which corresponds to an illuminating beam with a TEM$_{00}$ Gaussian profile. This is a smooth, uniform laser spot which neglects any fine-scale structure that might exist on the beam, caused by the telescope obscuration, for example. However, any fine-scale structure, if present, would not change the width of the Fizeau fringe because it would be smoothed out by the Fizeau response function. What would have an impact on the fringe width would be a laser spot that is wider than expected or one with sidelobes outside of the central spot. We note, however, that light backscattered from sidelobes would be blocked by the field stop and not lead to an increase in fringe width. Further details are discussed in the Appendix A3 and A4.

On examination, the fringes for FOV = 500 µrad (Fig. 6b) are all reasonably symmetric. Most notably, the secondary maximum shown for the comparable plane-wave fringe at AOI = 300 µrad has been completely smoothed out (compare the purple fringes in Fig. 6a and b). Increased broadening and peak shift for large AOI is evident and particularly strong for positive AOIs, as shown in Fig. 7.

Note that the width is FWHM and the shift is calculated as the mid-point of the width, which provides a good measure of the centre of energy for a fringe having any slight asymmetry. Note also that the energy within the fringes is essentially constant for different AOI values: the calculated changes across the full range are less than 1 %. For both width and shift,

the minimum values occur at an AOI close to −100 µrad and not normal incidence. This characteristic has been discussed by Langenbeck (1970) and summarized by McKay (2002), who showed that the optimum angle for illuminating a Fizeau wedge is tilted away from the apex (negative sign). Equivalent investigations for variation of y tilt, with x tilt = 0, showed similar results although, in this case, independent of the sign of tilt angle, with frequency shifts and broadening smaller by a factor of ≈ 0.6.

Extensive analyses, by ratio techniques and subsequent profile matching, showed that the fringes shown in Fig. 6b are well fitted by Voigt functions. The two examples for the optimum position with AOI = −100 µrad (x tilt = y tilt = 0) and for AOI = 300 µrad are shown in Fig. 8a and b, respectively, together with fits of a Lorentzian according to Eq. (2) (light-blue line) as well as a Voigt profile according to Eq. (5) (purple line). The respective FWHM values derived from the Voigt fit are given in the insets.

The better quality of the Voigt fit is particularly notable for AOI = 300 µrad (Fig. 8b). It can also be seen that an increase in the AOI increases the overall width by mainly increasing the Gaussian component of the Voigt profile. In particular, for AOI = −100 µrad, the Voigt profile has a width of $\Gamma_V \approx 98.2$ MHz, being composed of $\Gamma_G \approx 27.4$ MHz and $\Gamma_L \approx 90.0$ MHz. On the other hand, for AOI = 300 µrad, the Voigt profile has a width of $\Gamma_V \approx 150.8$ MHz, being composed of $\Gamma_G \approx 89.7$ MHz and $\Gamma_L \approx 95.3$ MHz.

The evolution of the respective Lorentzian and Gaussian contributions depending on AOI is illustrated in Fig. 9 for the full set of fringes shown in Fig. 6b.

Notably, the Lorentzian component (magenta) remains almost constant within the range 95 to 100 MHz FWHM, whereas the Gaussian component (blue) increases from ≈ 20 MHz at AOI = −200 µrad to 90 MHz for AOI = 300 µrad (see also Fig. 8b). Typically, the error limits on these values are less than ≈ 2 MHz but somewhat larger for smaller Gaussian components of < 30 MHz.
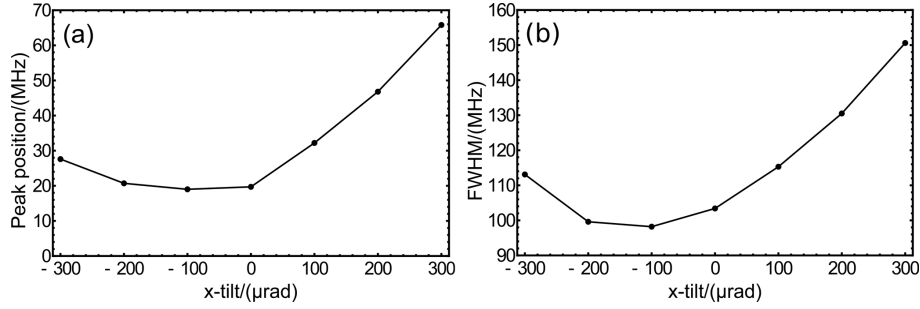
Figure 7. Fringe shift **(a)** and FWHM **(b)** for the modelled fringes shown in Fig. 6b. Note the minima for both curves close to AOI = −100 μrad.
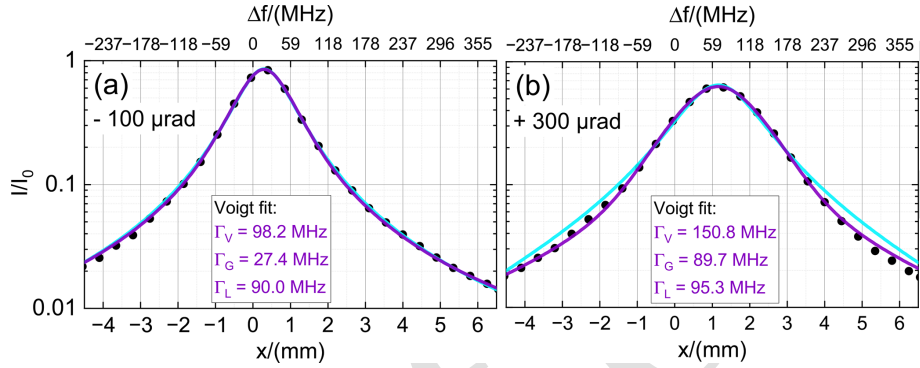
Figure 8. Modelled fringes (dots) for FOV = 500 μrad and x tilt AOI = −100 μrad **(a)** and AOI = 300 μrad **(b)**. Corresponding best fits of a Lorentzian (Eq. 2) and a Voigt profile (Eq. 5) are indicated by the light-blue and purple lines, respectively. The FWHM obtained from the Voigt fit are given in the inset. The y axes are in log scale to visualize the improved fit of the Voigt profile to the strongly Gaussian broadened fringe in panel **(b)**.
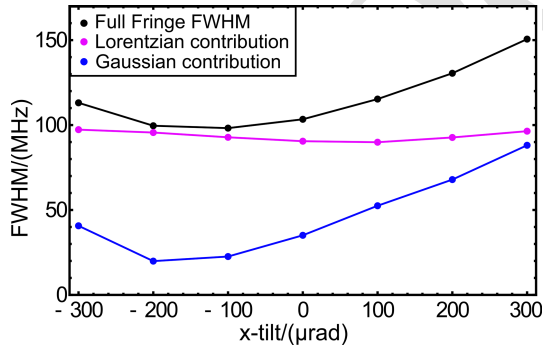
Figure 9. The Lorentzian (magenta) and Gaussian (blue) components derived by Voigt profile analysis of the modelled fringes shown in Fig. 6b.

It is thus clear that the increase in overall fringe width from ≈ 100 to 150 MHz is due to the increasing Gaussian component at larger AOIs, for the given FOV. Indeed, an AOI approaching 400 μrad (as evident for the Aeolus Fabry-Perot channel Witschas et al., 2022b) would give a full fringe width of about 175 MHz FWHM, with a Gaussian component somewhat greater than ≈ 115 MHz. Note that these val-

ues have still not incorporated the laser Gaussian pulse width of 45 MHz, as discussed in the following subsection.

4.3 Incorporation of laser pulse into Fizeau profile

The underlying rationale of the present investigation is to develop a more complete physical understanding of the Fizeau fringe and its composition. The two previous subsections have established, somewhat unexpectedly, the dominant Gaussian nature of two large contributions – the laser pulse and the impact of the AOI and FOV. There would be every expectation that, on folding these contributions into the complete Fizeau profile, their respective elements would combine together in the usual manner for Gaussians, i.e. by the root sum of squares. Nevertheless, it was considered valuable and constructive to investigate this and to both test the modelling/analytic procedures and promote confidence therein.

The laser pulse was considered a Gaussian profile with $\Gamma_G = 45$ MHz and with unit power. This was convolved in the modelling process with two fringe profiles drawn from Fig. 6b, with AOI = −100 μrad and AOI = 300 μrad and FOV = 500 μrad. The resultant profiles are shown in Fig. 10, with the originals shown in black and the convolved fringe shown in magenta. The y scale of intensity is normalized

against I_0 as the incident intensity on the plates and incorporates a representative value for plate absorption of 0.006 (together with $R = 0.88$).

As expected, the slight increase in FWHM, along with the decrease in peak height, for the convolved fringe is apparent.

4.4 Plate defects and fringe skewness

Early wave-optic modelling of ideal sinusoidal circular plate defects (± 0.5 to ± 4 nm on both plates) showed cyclic frequency shifts of up to ± 2 nm and gross fringe asymmetry as well as secondary maxima for defects larger than $\approx |2$ nm$|$. Somewhat later, an interferometric map of one set of plates became available and showed small-scale cyclic variations (in optical path separation) in the range from ± 0.5 to ± 1.5 nm, which were furthermore overlaid on large-scale changes of up to 5 nm.

This measured topography was modelled, and a set of three representative fringes are shown in Fig. 11.

Analysis shows small-scale frequency shifts of ± 1 MHz and, in addition, larger-scale variations of up to ≈ 14 MHz. On further examination, the two broadened fringes in Fig. 11 are not precisely vertical (i.e. are skewed), with equivalent frequency shifts from top to bottom of ≈ 63 MHz (a) and ≈ 31 MHz (b). It is readily shown that this skewness would give an equivalent width "top-hat" broadening function, with impact that closely matches the increased widths of profiles (a) and (b) compared with (c). The skewness shift of ≈ 63 MHz is also consistent with a shift of resonant frequency given by $(2\partial d/\lambda) \cdot \Gamma_{\mathrm{FSR}} \approx 60$ MHz, for a large-scale plate separation defect of $\partial d \approx 5$ nm, compared with the plate separation of 68.5 mm. This in turn leads to the fact that the Aeolus Fizeau fringe width changes with wedge position, i.e. with frequency. The impact of the fringe skewness on the wind retrieval of the Aeolus Airborne Demonstrator was also discussed by Lux et al. (2022).

4.5 The impact of Rayleigh–Brillouin scattering

At low levels of aerosol Mie scattering, the signal output from the Fizeau interferometer is increasingly dominated by broadband molecular RB scattering. Such scattering is typically of width in the range from 3.4 to 4.3 GHz FWHM, depending upon altitude, or rather pressure p and temperature T, and is of near Gaussian spectral shape (Witschas et al., 2010; Witschas, 2011a, b, 2012). In consequence, the measurement accuracy of Doppler shifts from small aerosol signals is strongly impacted by the broadband background signal for low-level aerosol signals. It is thus important to have good knowledge of the spectral distribution and strength of this background as it appears in the Fizeau output.

Figure 12a shows a Gaussian profile of representative width 3.8 GHz ($p = 100$ hPa, $T = 274$ K, $\lambda = 355$ nm), to be convolved at mid-order with the Fizeau instrument of 100 MHz FWHM and $\Gamma_{\mathrm{FSR}} = 2.2$ GHz. Full account is taken

of the overlap from successive orders at ± 1 FSR, ± 2 FSR, etc. It is instructive to consider this overlap of orders a little further. In Fig. 12b, the central peak of zero order (black) is shown with first order (purple) and second order (light blue). Their successive summation is shown in figure Fig. 12c, where the purple line indicates the summation of zero and first order, and the light-blue line indicates the further addition of the second order. It is important to notice that the resultant background (light blue) is essentially flat with relative intensity of 1.84, compared with the zero-order peak.

4.6 Summary of line broadening factors

From the extensive analysis of actual Aeolus fringe profiles in Sect. 3, and the modelling and simulation studies of the present section (Sect. 4), it is evident that two primary factors determine the width and spectral shape of the Fizeau fringe. These are firstly the Gaussian shape of the laser pulse and secondly the interaction at the Fizeau interferometer of the large AOI and FOV that contribute large Lorentzian and Gaussian spectral components. The following section (Sect. 5) investigates, at a fundamental theoretical level and from the evaluation of characteristic Aeolus fringes, how the actual width and spectral shape affect the measurement accuracy.

5 Impacts on the wind measurement accuracy

5.1 Impact of line broadening on fringe shift and Doppler wind measurement accuracy

5.1.1 Quantum-limited accuracy and SNR analysis of fringes

We consider, first, the accuracy of frequency estimation in the case of a fringe where there is no background light and the only noise source is shot noise on the signal photoelectrons. The following result for the standard deviation of frequency estimates δf was derived by Vaughan (1989, Appendix 10):

$$\delta f = \frac{C \cdot \Delta f}{\langle N_S \rangle^{1/2}}, \tag{9}$$

where Δf is the FWHM of the ultimate signal profile emerging from the instrument before detection, and the term in the denominator is the square root of the signal energy within the profile, expressed as the mean number of electron-counts $\langle N_S \rangle$ for a measurement ensemble. C is a constant of order 1, which depends on the actual spectral shape of the fringe. The derivation of Eq. (9) was based on determining the median position of the fringe (i.e. with equal numbers of photodetections on either side). By doing so, the constant C was shown to be $C_{\mathcal{L}} = \pi/4 \approx 0.785$ for a Lorentzian profile and $C_{\mathcal{G}} = [\pi/(16 \cdot \ln 2)]^{1/2} \approx 0.532$ for a Gaussian profile (see also Eqs. A94 and A95 in Vaughan, 1989). Note that there is an error in this reference, whereby the values given are
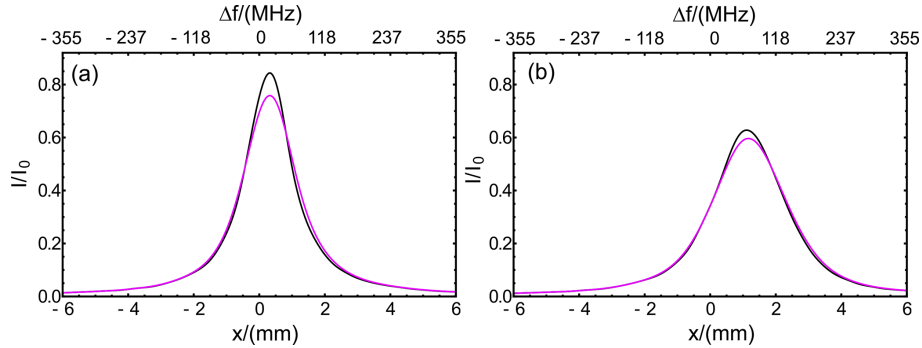
Figure 10. Fringe profiles modelled before (black) and after (magenta) convolution with a Gaussian laser pulse profile of 45 MHz FWHM. **(a)** AOI $= -100\,\mu$rad and FOV $= 500\,\mu$rad. **(b)** AOI $= +300\,\mu$rad and FOV $= 500\,\mu$rad.
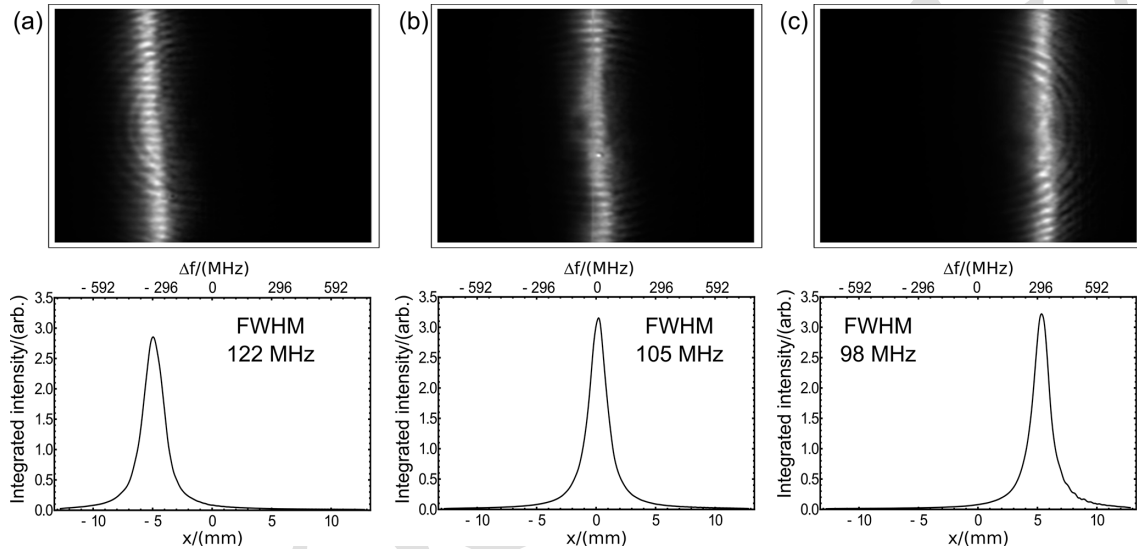
Figure 11. Modelled Fizeau fringes using the measured plate topography for a set of plates, as shown in the top-row images. Note the breakup of the fringes, characteristic of small-scale, semi-regular, groove defects and the fringe tilt (skewness) most evident in fringe **(a)**, attributable to larger-scale defects from top to bottom of the plates. The corresponding vertically integrated fringe profiles as well as their FWHM are shown in the bottom row.

greater than they should be by a factor of $\sqrt{2}$, as only one part of the fringe was considered for the derivation. The correct values are the ones we use here. The constant for a Voigt-shaped fringe $C_{\mathcal{V}}$ lies between the two values given above, depending on the respective Lorentzian and Gaussian contributions.

Now, Eq. (9) has the same functional form as the Cramér–Rao lower bound (CRLB) for this frequency estimation scenario, the only difference being the value of the multiplying constant. The CRLB is a value of the standard deviation which cannot be bettered by any unbiased frequency estimation method. The CRLB for a Gaussian profile is given in Rye (1998) by their Eq. (18). After converting their Gaussian $1/e^2$ radius to a FWHM, it is found that the CRLB multiplying factor is 0.425. If one does the same calculation for a Lorentzian profile, the result is a multiplying fac-

tor of $\sqrt{2} \approx 0.707$. It is not surprising that these multiplying factors are somewhat lower than those given by Vaughan (1989), since the former represent an ultimate limit and the latter come from an analysis of an actual frequency estimation algorithm. We use the latter approach here and, as will be seen, find good agreement with frequency estimation using least squares fitting to a defined profile.

In the ideal formulation given by Eq. (9), it is supposed that the electron counts N_S are free of spurious noise, dark current, and additional background signal. Consequently, the Poisson quantum-limited noise for the mean signal is equal to $\langle N_S \rangle^{1/2}$. In Eq. (9), the final term may be usefully considered as the SNR of the system, i.e.

$$\text{SNR} = \frac{\langle N_S \rangle}{\langle N_S \rangle^{1/2}} = \langle N_S \rangle^{1/2}, \tag{10}$$
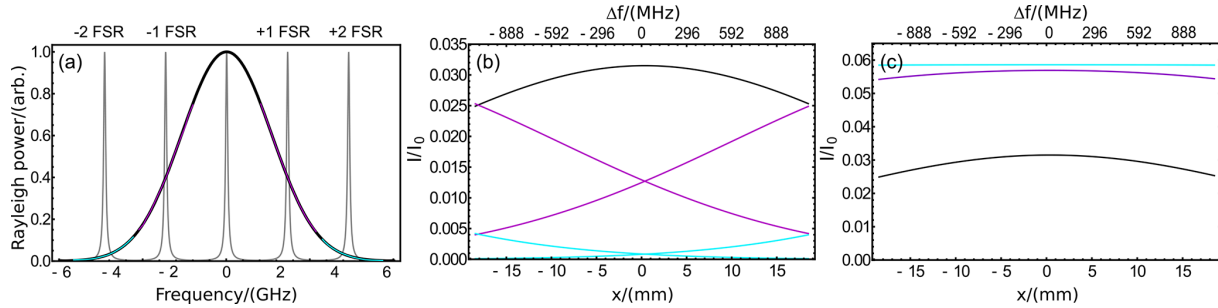
Figure 12. (a) Gaussian profile of 3.8 GHz FWHM ($p = 100$ hPa, $T = 274$ K, $\lambda = 355$ nm), as representative of a Rayleigh–Brillouin spectrum, for convolution with the Fizeau instrument function of 100 MHz FWHM and FSR = 2.2 GHz, sketched by the light-grey line. **(b)** Illustration of the overlap across one FSR for successive Gaussian profiles set at the centre, i.e. zero order (in black), ± 1 FSR (magenta), and ± 2 FSR (light blue). The respective regions are also highlighted in panel **(a)**. **(c)** Summation of successive orders. For all three orders this is essentially flat (light blue). Note the intensity ratio for the summed orders is 1.84 times the central order.

and hence, Eq. (9) can be transformed to

$$\delta f = \frac{C \cdot \Delta f}{\text{SNR}}. \tag{11}$$

Inspection of Eqs. (9) and (11) implies the paramount importance of the spectral line width Δf for the measurement accuracy and the evaluation of δf. As a simple example, a 2-fold spectroscopic reduction in Δf would be equivalent, in terms of accuracy, to a 4-fold energy increase in $\langle N_S \rangle$, requiring either an increase in the telescope diameter by a factor of 2 or an increase in the laser pulse energy by a factor of 4.

5.1.2 Fizeau fringe modelling and simulation

In Fig. 13a, two Fizeau fringes following an ideal Lorentzian profile according to Eq. (2) with $\Gamma_{\mathcal{L}} = 100$ MHz (1.69 mm) are shown. A total of 800 photoelectrons (black dots) and 3200 photoelectrons (light-blue dots) are distributed across 512 sampling points. The number of 512 points was chosen to give a much larger number of pixels across the fringe profile, so that the results can be compared with expressions such as Eq. (9), which are derived on the assumption of negligibly small pixels. The mean number of photoelectrons is proportional to the fringe profile shown by the solid line. The sample contents, i.e. the ordinates N_S, are random numbers taken from generated Poisson distributions. For the analysis of the simulated fringes, a non-linear square fit of Eq. (2) was applied, using the centre position x_0, the FWHM $\Gamma_{\mathcal{L}}$ and the area under the peak $\mathcal{I}_{\mathcal{L}}$ as free fit parameters.

The statistical variations in the centre frequency estimate were investigated for 1000 different realizations of the Poisson-distributed shot noise. The resultant histograms, with bin widths of 1.5 MHz, are shown in Fig. 13b. The zero-frequency point is taken to be the centre of the fringe. Note that the plotted histogram is a discretized version of the probability density, where the probability of a value lying within a given histogram bin is the height of the bin multiplied by

its width. Thus, the width of the histogram gives a measure of the accuracy of the frequency estimates. For the shown data, the root mean square (rms) and, hence, the standard deviations of these frequency estimates is 2.7 MHz (black, 800 photoelectrons) and 1.4 MHz (light blue, 3200 photoelectrons), which corresponds to a wind velocity error in horizontal LOS (HLOS) direction of 0.79 and 0.41 m s^{-1}, considering the conversion of 1 m s^{-1} HLOS wind speed to 3.43 MHz frequency shift, as resulting from the Doppler equation and considering a off-nadir angle of 37.6°.

This calculation, with 1000 estimations per set, was repeated for eight different values of the mean number of electron counts $\langle N_S \rangle = (1, 2, 4, 8, 16, 32, 64, 128) \times 10^2$. The rms values δf_{rms} of the eight resultant histograms of fringe centre (per Fig. 13c) were closely proportional to $\langle N_S \rangle^{-1/2}$. Expressed in terms of fringe width, Δf, the best-fitted curve according to Eq. (9) (Fig. 13c, black line) yields a $C_{\mathcal{V}}$ value of 0.788, which is in close agreement with the numerical value for a Lorentzian profile (0.785), as mentioned above.

5.2 Impact of Rayleigh–Brillouin background signal on the SNR and the measurement accuracy

5.2.1 Fringe simulation and modelling with significant background

In reality, the aerosol Mie peak in the Fizeau will sit on top of a pedestal of Rayleigh background. Even if this background is entirely uniform, shot noise on the background photoelectrons will degrade the performance of the fringe measurement. This situation was modelled by adding a flat pedestal to the fringe pattern and then calculating mean photo-electron numbers and shot noise realizations as before. The size of the pedestal was characterized by the mean number of background photoelectrons N_{ped} per pixel column. With 16 columns across the detector, the total number in the background is obviously $16 \times N_{\text{ped}}$. The simulation analysis includes the impact of the detector pixelation, and the fre-
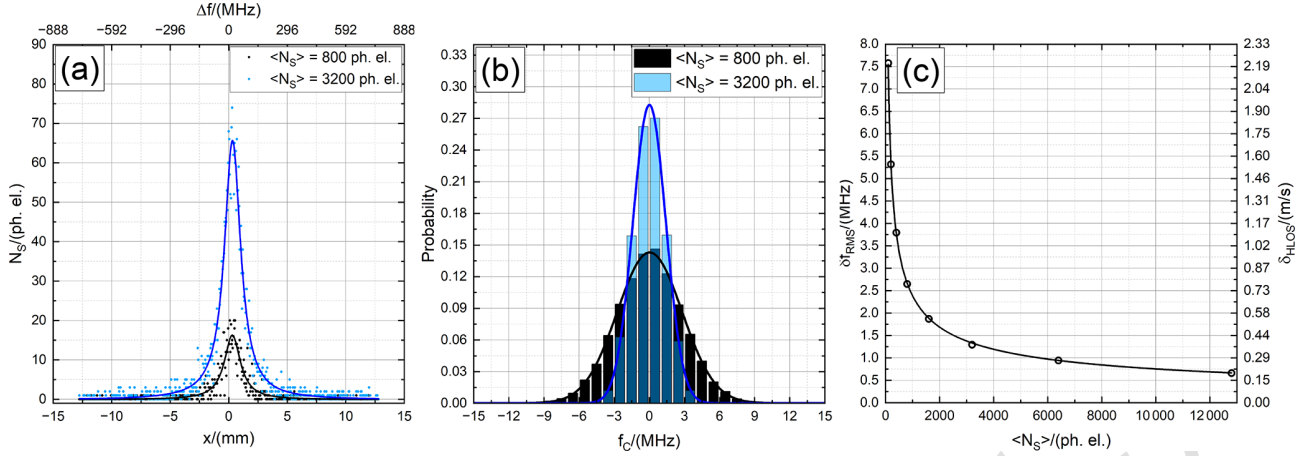
Figure 13. (a) Example of two Fizeau fringes (ideal Lorentzian profile) with $\Gamma_{\mathcal{L}} = 100\,\text{MHz}$ and shot noise (points). A total of 800 photoelectrons (black dots) and 3200 photoelectrons (light-blue dots) are distributed across 512 sampling points, and the solid lines indicate corresponding best fits of a Lorentzian. **(b)** Histogram for 1000 different realizations of centre frequency for the individual fitted Lorentzians. **(c)** Root mean square of the frequency estimates given for the frequency (left y axis) and HLOS wind speed (right y axis). The black line indicates a best fit of Eq. (9) to the data ($\Delta f = 100\,\text{MHz}$).

quency estimation algorithm was modified to account for a background pedestal of unknown height, adding and offset term to Eq. (2) as a free fit parameter. The number of realizations used to analyse the statistics was increased to 10000.

5 This early investigation was made as realistic as possible by selecting fringe parameters close to those expected for Aeolus at the time. These values have now largely been superseded, but the study itself proved very instructive and produced valuable guidelines for much of the following work.

10 The modelled Fizeau fringe was of width $\Delta f = 158.7\,\text{MHz}$, made up of a Lorentzian with $\Gamma_{\mathcal{L}} \approx 148\,\text{MHz}$ (close to the expected sum of Fizeau instrumental and laser pulse width), and a small Gaussian component, due to FOV speckle broadening, estimated at $\Gamma_{\mathcal{G}} \approx 25\,\text{MHz}$.

15 The main signal N_S was set at 1600 photoelectrons, and a wide range of N_{ped} up to 6750 photoelectrons per detector column were examined. Figure 14a shows a set of 10000 frequency estimates for the pedestal $N_{\text{ped}} = 6400$ photoelectrons (black) and for $N_{\text{ped}} = 1600$ photoelectrons (blue). In

20 panel (b), the corresponding histograms are shown in sets of width $5\,\text{m s}^{-1}$ (bars); the blue and black curves indicate each Gaussian fit, establishing that the frequency estimates are close to a normal distribution. In panel (c), the standard deviations of the frequency estimates for 10 different

25 pedestal levels are depicted. Note that for $N_{\text{ped}} = 1600$, the simulated SD value of small $\delta f_{\text{sim}} = 7.7\,\text{MHz}$ is equivalent to an HLOS Doppler velocity accuracy of $\delta v_{\text{HLOS}} \approx 2.2\,\text{m s}^{-1}$. For $N_{\text{ped}} = 6400$, the simulated SD value of small $\delta f_{\text{sim}} = 13.8\,\text{MHz}$ is equivalent to an HLOS Doppler velocity accu-

30 racy of $\delta v_{\text{HLOS}} \approx 4.0\,\text{m s}^{-1}$. This means that background signals of this order could in principle explain the random error as obtained for Aeolus. However, the actual N_{ped} levels are

in fact more than 40 times smaller than the large 6400 photoelectrons considered in this example.

5.2.2 Fringe calculations

This section presents an analytical framework that seeks to complement the extensive simulation and computations of the previous sections, as illustrated in Figs. 13 and 14. When there is a significant background pedestal present, a very basic SNR may be simply defined as

$$\text{SNR}_{\text{basic}} = \frac{N_S}{\left(N_S + m \cdot N_{\text{ped}}\right)^{1/2}}, \tag{12}$$

with m set equal to the total number of detector channels ($m = 16$); the noise term (denominator) in the bracket is the total number of photoelectrons recorded across the detector. Simple calculation of Eq. (12), comparable to the simulations and computation of Fig. 14, with similar large values of N_{ped}, illustrates its relative crudity. In particular, for $\langle N_S \rangle = 1600$ photoelectrons and $N_{\text{ped}} = 1600$ photoelectrons, $\text{SNR}_{\text{basic}} = 9.7$, equivalent to a error of $\delta f = 12.4\,\text{MHz}$. For the case with the even larger background signal of $N_{\text{ped}} = 6400$ photoelectrons, $\text{SNR}_{\text{basic}} = 5.0$, equivalent to an error of $\delta f = 24.2\,\text{MHz}$.

These values are notably larger errors than those values shown in Fig. 14b of 7.7 and 13.8 MHz, respectively. On reflection, this is hardly surprising: the bulk of the signal is contained within a small number of central channels, while the outer channels are dominated by the pedestal noise background. This simply illustrates the well-known spectroscopic principle of minimizing any analytic or search bandwidth f_{AB} in order to maximize SNR and improve signal accuracy. The question then is as follows: what analytic formulation
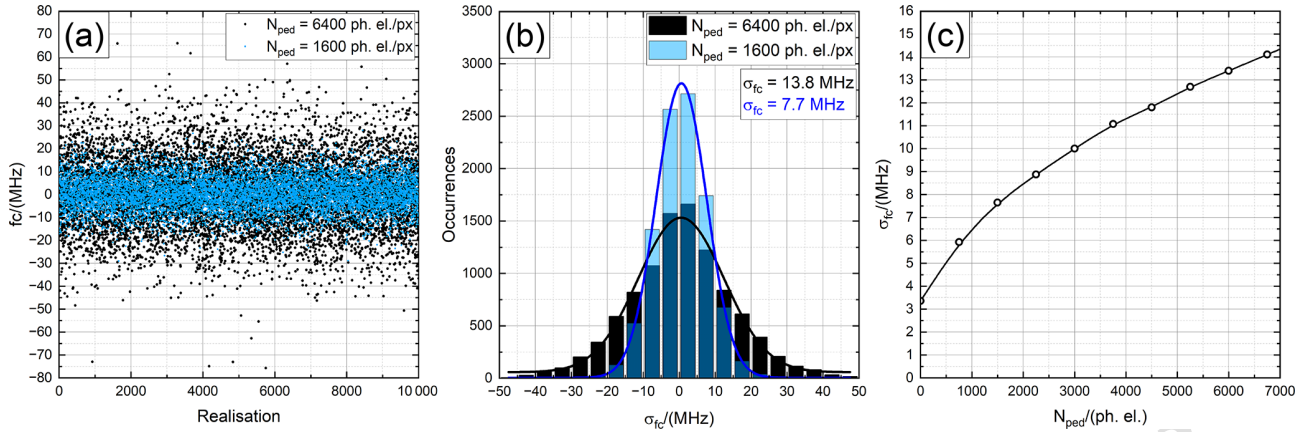
Figure 14. (a) Set of 10000 frequency estimates for a pedestal of 6400 background photoelectrons per detector column (black) and of 1600 background photoelectrons per detector column (blue) simulated with a fringe of width $\Delta f = 158.7\,\text{MHz}$ and a signal level of $N_S = 1600$. **(b)** Corresponding histogram of the data shown in panel **(a)** (bars) and related Gaussian fits (lines). The standard deviation of the data is indicated by the inset. **(c)** Standard deviation of frequency estimates versus mean number of pedestal photoelectrons per detector column. The mean number of signal photoelectrons for all cases is 1600.

of SNR would provide accuracy values closer to those of the simulation and computation procedures of the previous sections? A physically reasonable refined SNR, for insertion in Eq. (11), is

$$\text{SNR}_{\text{refined}} = \frac{k_\text{r} \cdot N_S}{\left(k_\text{r} \cdot N_S + n \cdot N_{\text{ped}}\right)^{1/2}}, \tag{13}$$

where k_r is the fraction of N_S contained within an effective analytic bandwidth f_{AB}, selected for purposes of calculation as $f_{\text{AB}} = r \cdot \Delta f = n \cdot \Gamma_{\text{TH}}$, with n being the number of pixels covered by the analytical bandwidth. Hence, r is the ratio of the analytical bandwidth f_{AB} and the fringe width Δf. It is worth mentioning that the SNR calculation by means of Eq. (13) differs from the one used in the Aeolus processor. However, it provides a good method for investigating the Mie wind performance evolution for varying instrumental parameters as it is shown in the following.

Calculated values of $\text{SNR}_{\text{refined}}$ obviously depend on the selected values of r. For best accuracy, the optimum choice would provide the largest possible $\text{SNR}_{\text{refined}}$, using the experimentally defined values N_S, N_{ped}, and Δf. By inserting typical Aeolus parameters, it is readily shown for $N_S \approx N_{\text{ped}}$, that plots of $\text{SNR}_{\text{refined}}$ versus r exhibit a broad profile, typically peaking in the range $r \approx 1.5$ to $r \approx 2.3$, with $\text{SNR}_{\text{refined}}$ remaining within $\approx 4\%$ of the maximum over the much broader range ($r = 1.2$ to $r = 3.0$).

The utility of $\text{SNR}_{\text{refined}}$ for relatively large N_{ped} is simply demonstrated in reference to the data of Fig. 14. As noted, this profile of $158.7\,\text{MHz}$ (FWHM) has a small Gaussian component. It is estimated that approximately 90% of the full Voigt width is due to the much larger Lorentzian component. Extensive analysis and modelling shows that the equivalent C coefficient results in $C_\mathcal{V} = 0.755$, for this case; a near optimum value of r is ≈ 1.6, i.e. an analytic bandwidth of

$\approx 250\,\text{MHz}$, equivalent to $n = 2.5$ for $\Gamma_{\text{TH}} = 100\,\text{MHz}$. The resultant value of k_r is ≈ 0.67.

Insertion of these values in Eqs. (11) and (13) gives $\text{SNR}_{\text{refined}} = 15.0$ equivalent to $\delta f = 8.0\,\text{MHz}$ ($N_S = 1600$ photoelectrons and $N_{\text{ped}} = 1600$ photoelectrons) and $\text{SNR}_{\text{refined}} = 8.2$ equivalent to $\delta f = 14.6\,\text{MHz}$ ($N_S = 1600$ photoelectrons and $N_{\text{ped}} = 6400$ photoelectrons). Obviously these analytic values of δf in Eq. (13) are much closer to the simulated values shown in Fig. 14 than those due to $\text{SNR}_{\text{basic}}$ shown in Eq. (12). The small residual discrepancies of $\approx 5\%$ is readily accounted for by uncertainty in the precise Lorentzian fraction. For a better comparison, the resulting $\text{SNR}_{\text{basic}}$ and $\text{SNR}_{\text{refined}}$ as well as the corresponding error for the two cases discussed in Fig. 14 are summarized in Table 2.

The foregoing analytic procedure, which will be described in detail and applied in a forthcoming publication, offers a relatively simple, easily calculated representation of the quantum-limited accuracy for direct detection spectroscopic systems. It thus provides a useful metric for comparison of potential performance for variation of instrumental parameters. However, caution is needed in comparing different analytic techniques, via their apparent SNRs.

5.3 Measurement accuracy with the Aeolus Fizeau interferometer and potential improvements for future applications

5.3.1 Aeolus experimental performance

For over 4 years in orbit, the Fizeau instrument, primarily intended as a technical demonstrator, has in fact provided an enormous volume of wind data of great value for meteorological analysis (Rennie et al., 2021; Rennie and Isaksen,

Table 2. Comparison of derived $\text{SNR}_{\text{basic}}$ (Eq. 12) and $\text{SNR}_{\text{refined}}$ (Eq. 13) and corresponding δf (Eq. 12) for different $\langle N_S \rangle$ and N_{ped} values ($\Delta f = 158.7\,\text{MHz}$, $C_V = 0.755$, $m = 16$, $n = 2.5$, $k_r = 0.67$).

	$\text{SNR}_{\text{basic}}$	δf	$\text{SNR}_{\text{refined}}$	δf	δf from Fig. 14
$\langle N_S \rangle = 1600$ photoelectrons, $N_{\text{ped}=1600}$ photoelectrons	9.7	12.4 MHz	15.1	8.0 MHz	7.7 MHz
$\langle N_S \rangle = 1600$ photoelectrons, $N_{\text{ped}=6400}$ photoelectrons	5.0	24.2 MHz	8.2	14.6 MHz	13.8 MHz

2024). The principle experimental main findings of the Aeolus Fizeau system throughout its operation may be summarized as follows.

1. The estimated precision of the HLOS winds varied considerably during the mission and with geolocation, season, processing software version, and range-bin settings, particularly for the Rayleigh-clear HLOS winds but to a much smaller extent for the Mie-cloudy winds with random errors varying from 2.5 to $3.6\,\text{m s}^{-1}$ (HLOS) on horizontal scales of about 10 to 20 km (Rennie and Isaksen, 2024). It is worth noting that HLOS winds are the LOS winds projected to horizontal direction. Considering the Aeolus pointing angle of $37.6°$, $1\,\text{m s}^{-1}$ HLOS wind corresponds to 3.43 MHz Doppler frequency shift.

2. A significant fraction of the valid Mie-cloudy wind data resulted from strong backscatter from ice and water clouds, including cloud top and more diffuse thin clouds.

3. There were few measurements that may be attributed unequivocally to purely aerosol backscattering, and these were almost entirely due to rare high-backscatter events caused, for example by incipient cirrus cloud formation, volcanic eruption, dust plumes, and wildfire smoke being swept high into the atmosphere.

4. There were almost no observations of Mie winds with errors below $1\,\text{m s}^{-1}$ (HLOS), in contrast to the expectations from pre-launch simulations and specifications (ESA, 2016).

5. There were only small changes in performance for Mie-cloudy winds when switching between laser flight model A (FM-A) operation and laser FM-B, in contrast to the larger changes that were obvious for Rayleigh-clear winds due to the changing atmospheric path signal levels when operating with each of the lasers.

No clear reasons have been advanced for these discrepancies, but they appear to point to a considerable loss of radiometric performance. Conceivably, this might be due to loss of optical alignment accuracy and reduction in light signal through the optical train, for instance if the field-stop aperture is not positioned at the centre of the optical focus of the telescope, leading to an over-illumination of the field

stop. Indeed, this hypothesis would be supported by the large apparent AOI, of order 300 to 400 µrad, needed to explain the large spectral line widths discussed in Sect. 3. However, also a larger beam diameter in the field stop due to larger wave-front errors of optics (e.g. the telescope) leads to over-illumination.

5.3.2 Calculation and analysis of the present Aeolus Fizeau performance

(a) Operational Fizeau parameters for fringe analysis. Considering the earlier discussions in Sects. 3 and 4, as well as an examination of the Aeolus Fizeau Mie profiles, it is considered that (before detection) these profiles are close to a Voigt profile with a FWHM of approximately 175 MHz. This profile is further described as consisting of an instrumental Lorentzian component of $\approx 95\,\text{MHz}$, as retrieved from the simulations shown in Fig. 8b, and a Gaussian component of $\approx 117\,\text{MHz}$, the latter resulting from the combination of 108 MHz (instrumental AOI aperture broadening) and 45 MHz (laser pulse width). Notably, when this Voigt profile is convolved with the detector's "top-hat" function of 100 MHz pixel width, the resulting prototype fringe has an FWHM of 205 MHz, which is very close to the one shown in Fig. 2b. From these values, the Lorentzian fraction is estimated as $\mathcal{L}_{\text{fraction}} = 95/175 \approx 0.54$, with a corresponding $C_V \approx 0.66$, resulting from numerical simulations similar to the one shown in Fig. 14. Using these values and following Eq. (13), extensive simulations of the SNR versus r reveal a weak, broad peak (not shown) which results in an optimal analytic bandwidth $f_{\text{AB}} = 300\,\text{MHz}$ (i.e. $n \approx 3$ pixels). This leads to a collection efficiency for the Mie signal of $k_r \approx 0.80$. For calculation and comparison in Eqs. (11) and (13), these values are considered as reasonably representative of Aeolus operation and are used in the following analysis.

(b) Analysis of strong signal Aeolus fringes. A group of strong signal fringes and associated data tables are shown in Fig. 15. These three sets of atmospheric observations were recorded on 1 June 2022 at around 06:00 UTC, each consisting of five measured Fizeau fringes. The fringes were accumulated over successive paths, with horizontal integration length of about 12 km and vertical integration length of 0.75 km and at different altitudes: (a) 8.45 km (range gate 12), (b) 4.7 km (range gate 17), and (c) 1.7 km (range gate 21). It must be appreciated that these sets have been taken as an example from the many millions of observations recorded

in the 4 years of operation, and as such, they are better considered "indicative" rather than "representative".

Examination of these fringes and associated data reveals two important points. First, the mean value of N_S is of the order of 1000 LSB, which corresponds to ≈ 1462 photoelectrons. It is worth noting that during the detection process, the amplified detector signal including DCO is converted into units of least significant bits (LSBs), and the conversion rate of this process is given by the radiometric gain of 0.684 LSB per photoelectron for the Mie ACCD detector (Lux et al., 2024). Hence, the fringes are based on a strong signal but fluctuate significantly, ranging from 0 to 2500 LSB across the 15 spectra. Second, the mean value of N_{ped} is ≈ 40 LSB (≈ 58 photoelectrons), which is more than an order of magnitude lower than some of the values calculated and modelled in the previous section; it is also significantly lower than anticipated for the Rayleigh–Brillouin background. This evidence offers further support for the hypothesis of reduced radiometric efficiency in Aeolus operation. However, for single realizations, it can also happen that the cloud top appears at the top of the range bin, which would result in a low Rayleigh background as well.

From the above data, 12 of the 15 fringes have $SNR_{refined} > 25$ and 3 have $SNR_{refined} \approx 50$, corresponding to standard deviation accuracies (per signal statistics) of $\delta_{v_{HLOS}} \approx 1.4\,\mathrm{m\,s^{-1}}$ and $\delta_{v_{HLOS}} \approx 0.7\,\mathrm{m\,s^{-1}}$, respectively. It is worth noting that for set (a), at high altitude 8.45 km, the spread in fringe centre x_c is only 0.041 px (4.1 MHz), equivalent to a range of measured HLOS velocities of $\approx 1.2\,\mathrm{m\,s^{-1}}$, close to the statistical value. In contrast, for set (b), the spread of 0.207 px was equivalent to a range of measured HLOS velocities of $\approx 6.0\,\mathrm{m\,s^{-1}}$; this might suggest increased shear and turbulence along the 70 km atmospheric path at this lower altitude of 4.7 km. It is further worth noting that the variation on the values of the derived N_{ped} of 36.4 LSB to 41.6 LSB, in set (a), are within ± 2 times the standard deviation (per Poisson statistics) of the mean value of 37.9 LSB. In contrast, the variation of N_{ped} at the lower altitudes (b) and (c) is well outside the Poisson values; this is probably due to variable levels of attenuation in the layers above.

In summary, these 12 measurements with notably strong signals suggest that in these cases the scattering is dominated by clouds. The fact that it is evident at all altitudes could indicate that the clouds are sufficiently thin and diffuse to permit adequate transmission to lower altitudes. The three examples stem from three different observations/profiles of the orbit. There could have been a thick cloud in different altitudes for each of the examples. However, it is more likely that it is largely due to scattered clouds of low overall coverage over the 12 km path per measurement.

(c) Analysis of weak signal Aeolus fringes. Examination of Aeolus data reveals that $\approx 50\%$ of the valid Mie winds from the Aeolus processor are retrieved with notably smaller SNR between 8.5 and 15. Note that this SNR, based on the Mie core 2 algorithm, is derived somewhat differently and

employs a Lorentzian fit. Hence, the values differ slightly from the $SNR_{refined}$ values presently employed.

For present purposes, five indicative low signal fringes have been taken from the same orbit as used in the previous subsection and are shown in Fig. 16. The associated data table shows smaller values of $SNR_{refined}$ ranging from 16.0 down to 12.4. These are equivalent to standard deviation values of $\delta f = 7.2$ and $\delta f = 9.3$ MHz, respectively, equivalent to $\delta_{v_{HLOS}} = 2.1$ and $\delta_{v_{HLOS}} = 2.7\,\mathrm{m\,s^{-1}}$. These values are indeed somewhat smaller than the range of errors of 2.5 to $3.6\,\mathrm{m\,s^{-1}}$ noted for Mie-cloudy winds (Rennie and Isaksen, 2024).

Examination of the spectra in Fig. 16 indicates that, in spectroscopic terms, these are still quite well defined fringes. It is generally considered that, for a semi-ideal stable system, a well defined SNR greater than ≈ 6 provides a reliable, statistically "valid" measurement, although the equivalent large error may make it "not useful for purpose". In the present case an $SNR_{refined}$ of 9 would lead to $\delta_{v_{HLOS}} = 3.6\,\mathrm{m\,s^{-1}}$, at the limit of acceptability and usefulness.

5.4 Potential improvements to the Fizeau measurement accuracy in the short and long term

During this investigation, it became apparent that technical and parametric changes to the Fizeau instrument would notably improve the wind measurement accuracy. The principal changes may be briefly summarized as the reduction in the actual fringe profile width as it emerges from the Fizeau, a correction of the radiometric efficiency (RME) signal loss factor as it was existing for Aeolus, and the introduction of additional optical pre-filtering to further reduce both Rayleigh–Brillouin and solar background. The following notes provide a basic outline of a potential accuracy improvement.

For simple comparison, the example of a rather weak signal, with accuracy $\delta_{v_{HLOS}} = 3.8\,\mathrm{m\,s^{-1}}$ at the outer limit of useful range, has been selected and is hence slightly worse than which would be expected from the fringes shown in Fig. 16. As is shown in the following, potential improvements on this value are then demonstrated to achieve notably better than $\delta_{v_{HLOS}} = 2.0\,\mathrm{m\,s^{-1}}$ and in future upgraded systems better than $\delta_{v_{HLOS}} = 1.0\,\mathrm{m\,s^{-1}}$.

5.4.1 Potential improvements within the framework of the Aeolus Fizeau parameters

In the following, four different scenarios, (a) to (d), with different Fizeau parameters are discussed regarding their corresponding wind accuracy.

(a) Per the operational Aeolus instrument. Consider the operational Aeolus Fizeau line width $\Delta f = 175$ MHz (at AOI $\approx 300\,\mu\mathrm{rad}$) with $N_S = 140$ LSB and background $N_{ped} = 30$ LSB per pixel, equivalent to about $N_S = 204.7$ photoelectrons and $N_{ped} = 43.9$ photoelectrons per pixel,
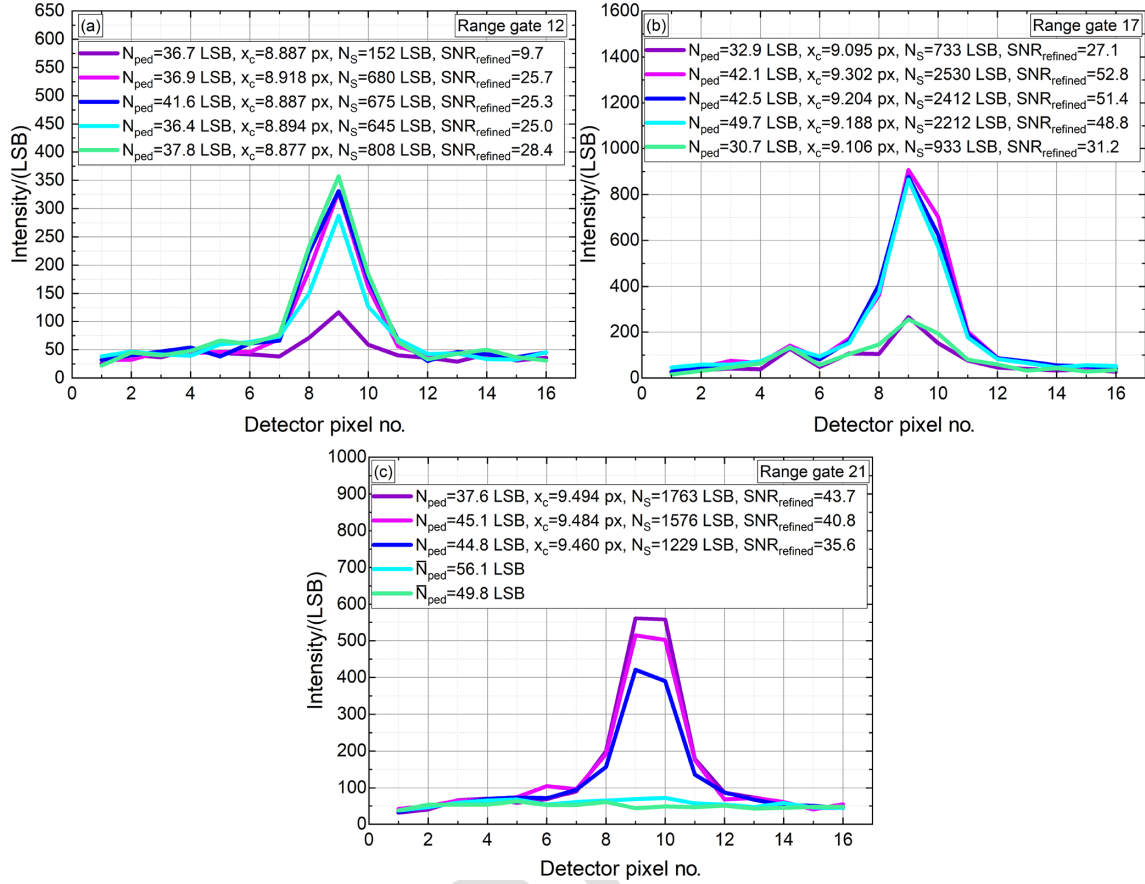
Figure 15. Three sets of five atmospheric fringe profiles recorded by Aeolus on 1 June 2022 at 06:00 UTC at different altitudes of 8.45 km corresponding to range gate 12 (**a**), 4.7 km (range gate 17, **b**) and 1.7 km (range gate 21, **c**). Derived data tables containing values of N_{ped} (per pixel), the centre position in pixels x_{c}, N_{S}, as well as the $\text{SNR}_{\text{refined}}$ (Eq. 13) using $\Delta f = 175\,\text{MHz}$, $C_{\mathcal{V}} = 0.66$, $k_r \approx 0.80$, and $n = 3\,\text{px}$ are given for each fringe by the respective inset.

considering the ACCD radiometric gain of 0.684 LSB per photoelectron. For the present and all following calculations of SNR and δf (per Eqs. 9 and 13), a mid-range set of representative parameters of $C_{\mathcal{V}} = 0.7$, $k_r = 0.8$ and $r = 1.8$ (defining the analytic bandwidth to be $r \cdot \Delta f$) have been selected. Insertion of these values leads to $\text{SNR}_{\text{refined}} = 9.4$, $\delta f = 13.0\,\text{MHz}$, and $\delta_{v_{\text{HLOS}}} = 3.8\,\text{m s}^{-1}$.

Taking account of the RME loss factor (for both N_{S} and N_{ped}), current expectation suggests this could lie in the range 2 to 3. For the present calculation, suppose a loss factor of 2.5. It is simply shown that the increase in $\text{SNR}_{\text{refined}}$ is $2.5^{(1/2)} = 1.58$. Hence, in the above values, the resultant accuracies become $\delta f = 8.2\,\text{MHz}$ and $\delta_{v_{\text{HLOS}}} = 2.4\,\text{m s}^{-1}$.

As a further step, consider optical pre-filtering applied to the input beam of the Fizeau interferometer to further reduce background and eliminate overlap of successive orders of RB scattering. If completely successful, this would have minimal effect on N_{S}, while reducing N_{ped} by a factor of ≈ 1.84. Further calculation leads to moderately improved $\delta f = 7.3\,\text{MHz}$ and $\delta_{v_{\text{HLOS}}} = 2.1\,\text{m s}^{-1}$. These three sets of values are indi-

cated in column (a) of Fig. 17, where the initial situation is indicated by the purple line, and the improvements for correction of the RME and optical pre-filtering are indicated by the dark-blue and light-blue line, respectively.

(b) Operate at the optimum AOI. With controlled operation at an optimum AOI of $\approx -100\,\mu\text{rad}$ to realize the minimum spectral line width (i.e. the so-called "sweet spot"), the Δf is reduced to $\approx 115\,\text{MHz}$. As shown in Fig. 6, the signal energies N_{S} and N_{ped} for different AOI values are essentially unchanged. Insertion of these values in Eqs. (9) and (13) leads to $\text{SNR}_{\text{refined}} = 10.3$, $\delta f = 7.8\,\text{MHz}$, and $\delta_{v_{\text{HLOS}}} = 2.3\,\text{m s}^{-1}$. Note the small increase in SNR due to the reduced background signal (with smaller analytic bandwidth) entering the equations. Compensation for the RME loss factor gives the accuracy values $\delta f = 5.0\,\text{MHz}$ and $\delta_{v_{\text{HLOS}}} = 1.5\,\text{m s}^{-1}$. With further incorporation of optical pre-filtering, the values become $\delta f = 4.5\,\text{MHz}$ and $\delta_{v_{\text{HLOS}}} = 1.3\,\text{m s}^{-1}$. These three sets of values are indicated in column (b) of Fig. 17.
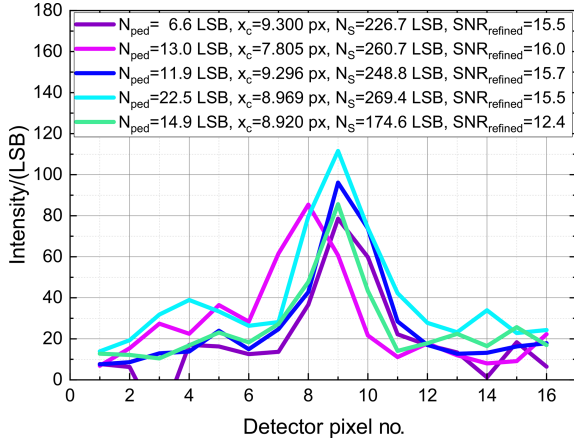
Figure 16. Five atmospheric fringe profiles recorded by Aeolus on 1 June 2022 at 06:00 UTC with an SNR varying between 10.4 and 15. The figure labels containing values of N_{ped}, the centre position in pixels x_c, N_S determined by a best fit of Eq. (5), the SNR$_{refined}$ (Eq. 13) using $\Delta f = 175$ MHz, $C_V = 0.66$, $k_r \approx 0.80$, and $n = 3$ px are given for each fringe.
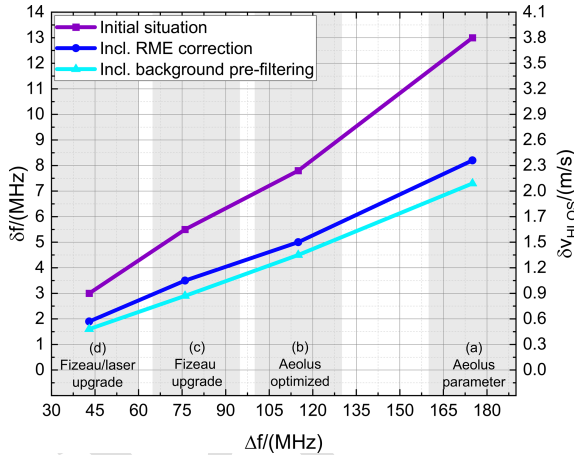
Figure 17. Wind measurement accuracy δf (left y axis) and $\delta_{v_{HLOS}}$ (right y axis), calculated for reasonable but low signal levels of $N_S = 204.7$ photoelectrons (140 LSB) and $N_{ped} = 43.9$ photoelectrons (30 LSB) for four sets (columns) of Fizeau instrumental parameters, calculated by means of Eqs. (9) and (13). $C_V = 0.7$, $k_r = 0.8$ and $r = 1.8$ is used for all cases. The initial situation is indicated by the purple line. Potential improvements for correction of the radiometric efficiency loss and optical pre-filtering are indicated by the dark-blue and light-blue line, respectively.

5.4.2 Potential performance of upgraded Fizeau systems with optimized parameters

Any upgraded system (for an Aeolus-type operation) must incorporate two vital considerations. Firstly, the meteorological specification requires a wind velocity measurement capability of up to ± 100 m s^{-1} in the HLOS direction (v_{HLOS}). This is typically equivalent to a v_{LOS} extending to ± 61 m s^{-1},

considering a off-nadir angle of 37.6°. Secondly, it is of paramount spectroscopic importance to maximize and maintain the signal collection of the narrow band at atmospheric Mie scattering. This necessarily requires careful consideration of spectroscopic factors of frequency dispersion (MHz per mm) at the plates (and equivalent fringe plane), as dictated by the Fizeau interferometer plate separation and wedge angle, together with appropriate plate reflectivity and fringe finesse. Two possible future systems are considered below.

(c) Reduce FSR and line width. With approximate doubling of the interferometer plate spacing to ≈ 135 mm (instead of 68.5 mm) and appropriate selection of wedge angle and finesse, the Mie signal collection efficiency and N_S may be maintained, and the overlap of orders as well as the value of N_{ped} per MHz is approximately doubled. A useful spectral range of about ± 400 MHz should readily be achievable to provide the required v_{HLOS} range of ± 100 m s^{-1}. In this case, the Fizeau instrumental profile would have a FWHM of ≈ 47 MHz (Lorentzian shape), which, after convolution with the laser pulse profile of ≈ 45 MHz (Gaussian shape), leads to a resultant fringe profile of $\Delta f = 76$ MHz.

Incorporation of these values into Eqs. (9) and (13) leads to SNR$_{refined} = 9.7$, $\delta f = 5.5$ MHz, and $\delta_{v_{HLOS}} = 1.6$ m s^{-1}. With the RME factor, these become $\delta f = 3.5$ MHz and $\delta_{v_{HLOS}} = 1.0$ m s^{-1}, and with further optical pre-filtering, $\delta f = 2.9$ MHz and $\delta_{v_{HLOS}} = 0.8$ m s^{-1}. These three sets of values are indicated in column (c) of Fig. 17.

(d) Further reduce FSR, line width, and laser pulse width. Considered purely a spectroscopic accuracy problem, there remain two powerful constraints on further advance. Firstly, the present laser pulse profile of width $\Gamma_G = 45$ MHz is now a major contributor to the fringe width Δf. Secondly, the meteorological requirement of v_{HLOS}, ranging over ± 100 m s^{-1}, requires a large useful spectral range. It is thus worth examining the "what if" question of reducing both.

Consider a laser pulse profile reduced to $\Gamma_G = 20$ MHz, which would require an increase in the laser pulse length from about 20 ns to 50 ns. With further increase in plate separation to ≈ 200 mm, a useful spectral range of about 280 MHz should be achievable, to provide a v_{HLOS} range of ± 72 m s^{-1}. With further appropriate selection of Fizeau parameters to maintain N_S, the resultant fringe profile would be $\Delta f \approx 43$ MHz, with approximate trebling of the RB background N_{ped} per MHz. Following the previous calculations, the accuracy values become SNR$_{refined} = 10.0$, $\delta f = 3.0$ MHz, and $\delta_{v_{HLOS}} = 0.9$ m s^{-1}. With the RME factor, these become $\delta f = 1.9$ MHz and $\delta_{v_{HLOS}} = 0.6$ m s^{-1}. With further optical pre-filtering, these become $\delta f = 1.6$ MHz and $\delta_{v_{HLOS}} = 0.5$ m s^{-1}. These three sets of values are indicated in column (d) of Fig. 17.

5.4.3 Comments and discussion of wind accuracy results

The most obvious feature of the accuracy values as represented in Fig. 17 is the rapid near-linear improvement with Fizeau fringe width Δf. In column (b), with operation at optimum AOI, $\delta_{v_{\mathrm{HLOS}}}$ has immediately reduced from 3.8 to $2.3\,\mathrm{m\,s^{-1}}$ and to $1.5\,\mathrm{m\,s^{-1}}$ with further RME correction.

In column (c), $\delta_{v_{\mathrm{HLOS}}} = 1.6\,\mathrm{m\,s^{-1}}$, and with further RME correction, it would become $1.0\,\mathrm{m\,s^{-1}}$, which is a factor of 3.8 improvement on the starting value. These gains in wind measurement accuracy are, of course, significant. However, possibly of greater significance is the prospect of considerably increased global coverage. Simple analysis shows that, to first order, similar factors of improvement would be achieved starting from very much larger and presently "not useful" values of $\delta_{v_{\mathrm{HLOS}}}$.

As obvious from Fig. 17, the final improvements in accuracy would be achieved with optical pre-filtering and a reduced laser pulse profile; it is worth considering their technical feasibility. Techniques of optical pre-filtering and FSR extension were extensively developed in the era of classical spectroscopy (for an early review, see, for instance, Chap. 6 in Vaughan, 1989). Investigation of possible techniques for the present Fizeau instrument would not be trivial but should be relatively low-cost without major impact on overall optical layout. However, reduction in the laser pulse frequency width would clearly involve a major and costly long-term programme. The existing Aeolus laser design concept is at least 25 years old. The present short temporal pulse length, about 20 ns, leading to a physical length of about 6 m and width about 50 MHz, is driven by laser engineering and the required high-peak power to provide high conversion efficiency in the frequency tripling process. Ideally, in the future, optimization of the balance of pulse length, conversion efficiency, and total pulse energy would seem desirable and, in performance terms, potentially cost-effective.

It is finally worth mentioning that the accuracies noted above are comparable to what may be achieved with heterodyne detection wind lidar, as, for instance, shown by Witschas et al. (2017, 2020, 2022a, 2023a). In Witschas et al. (2017) for instance, the standard deviation of the LOS wind speeds derived from an airborne heterodyne detection wind lidar is $\delta_{v_{\mathrm{LOS}}} = 0.2\,\mathrm{m\,s^{-1}}$.

6 Conclusions

In its 4.5 years of operation following its launch in August 2018, ESA's Aeolus mission has provided an enormous number of global wind lidar data. Initially intended primarily as a 3-year technical demonstrator, the mission quickly proved that the volume and quality of its data could significantly enhance current numerical weather prediction. Besides the Rayleigh-clear winds, that provided a much larger number of data, Mie-cloudy winds were shown to be of particular importance due to their higher precision and their availability in the boundary layer region.

Since its launch, the detailed spectroscopic operation of the Fizeau interferometer has been extensively investigated against a background of technical observation, revealing two important findings. Firstly, the apparent angles of incidence of the scattered return signal beam on the Fizeau interferometer were considerably larger than anticipated, reaching up to several hundred microradians (µrad), as clearly evidenced in the FPI-based Rayleigh channel (Witschas et al., 2022b). Secondly, the signal levels were lower than expected for both the Rayleigh and the Mie channels. From the Mie channel, viable returns were almost entirely due to strongly enhanced scattering from cloud top, thin diffuse cloud, volcanic aerosols, dust plumes, and smoke from forest fires, with virtually no viable signals from background aerosol.

The present investigation has thus concentrated on fundamental spectroscopic problems, with particular emphasis on studying the composition of the spectral line width from the Fizeau spectrometer and its impact on the SNR, fringe shift, and wind measurement accuracy at the quantum limit of performance, as expressed in Eq. (9). This analysis underscores the critical importance of minimizing spectral line width. In terms of measurement accuracy, a 2-fold reduction in line width is equivalent to a 4-fold increase in signal energy.

The study of Fizeau fringes from Aeolus operation establishes a large Gaussian shape contribution of $\approx 130\,\mathrm{MHz}$ (FWHM) to the instrumental profile, which consists of a Lorentzian $\approx 100\,\mathrm{MHz}$ (FWHM). Wave-optic analysis of fringe formation provides a convincing explanation for this effect, attributing it to the input signal beam's large AOI of $\approx 300\,\mathrm{\mu rad}$. This large angle also likely contributes to the observed loss of radiometric signal collection efficiency due to beam clipping at the small field stop aperture in the optical train. In contrast, operation closer to normal incidence greatly reduces the Gaussian component and should minimize any signal loss. The implications of these findings are discussed for several scenarios, including the optimization of present Aeolus Fizeau parameters, an upgraded Fizeau system, and an enhanced laser source. Projected improvements in wind speed measurement accuracy range from 1.8 to 7.2 times over the demonstrated Aeolus performance.

From a broad perspective, the present findings regarding the apparent misalignment of the signal beam, amounting to $\approx 300\,\mathrm{\mu rad}$, warrant further comment and discussion. This value is indeed large in the context of standard interferometric and spectroscopic practices. In a laboratory setting, where direct micro-adjustment is possible, misalignment errors of less than $10\,\mathrm{\mu rad}$ are typically expected. For Aeolus, the large and progressive changes in AOI in both the Rayleigh and Mie channels require analysis and explanation. It is also worth noting that if a misalignment of $\approx 300\,\mathrm{\mu rad}$ results in a signal loss of $\approx 60\,\%$, crude estimates suggest that a misalignment of $\approx 450\,\mathrm{\mu rad}$ could lead to losses exceeding

$\approx 90\,\%$, assuming the AOI is one of several potential root causes of the signal loss (though this remains unverified). For instance, The Pierre Auger Collaboration et al. (2024) noted that laser-induced contamination and laser-induced damage
5 are the most probable causes for the progressive observed signal loss during the mission and suggest that clipping accounts for less than 10 % of the loss during the analysed mission phase. They also mention that the initial loss mechanisms are still the subject of ongoing studies.
10 In conclusion, for future comparable lidar missions, it is desirable to address several questions arising from the Aeolus experience. These questions may include the following: what are the primary sources of alignment error in Aeolus? Are they attributable to distortions in the relatively com-
15 plex optical train. Would it be feasible and beneficial to incorporate active optical control and micro-alignment for the signal beams incident on the interferometers? Furthermore, could a robust space-qualified scheme be developed for this purpose?
20 It is also worth mentioning that the results and tools presented in this study might be useful for optimizing the specifications for the Mie channel of any Aeolus-like successor mission.

Appendix A: Wave-optics model

25 As mentioned in Sect. 3, the wave-optic Fizeau model was originally developed to investigate the effect of circular defects arising from the MRF process applied to the Fizeau plates (Vaughan and Ridley, 2013; Vaughan and Ridley, 2016). The impact of these on fringe formation was initially
30 modelled using the ray-optic approach, where the component of the transmitted field after the p passage through the Fizeau has a phase of (Born and Wolf, 1980)

$$
\delta_p = \frac{4\pi}{\lambda} h \cos(\theta) \frac{\sin\left[(p-1)\alpha\right]}{\tan(\alpha)} \left\{ \cos\left[(p-1)\alpha\right] - \tan(\theta)\sin\left[(p-1)\alpha\right] \right\}.
\tag{A1}
$$

Here, λ is the wavelength; h is the plate separation; α is the
35 wedge angle; and θ is the angle of incidence, defined to be positive when the incoming radiation is tilted away from the apex of the wedge. The circular defects from MRF polishing were modelled by a simple sinusoidal variation in the surface of one of the plates:

40 $h(x, y) = h_0 + h_g \cos \frac{2\pi r}{w_g},$ (A2)

where $r^2 = x^2 + y^2$. It can immediately be seen that there are some issues in applying Eq. (A1). The surface variations can be included via h and α, i.e. by treating α as a local effective wedge angle. However, this approach will not be
45 correct when there is a large plate separation or when θ departs significantly from zero, as it assumes a ray that comes from a particular location on the plate always returns close to that same location. For this reason, it was decided to investigate a wave-optics approach, as described in Sect. A1. A comparison between results using Eq. (A1) and corresponding wave-optic calculations is given in Fig. A1 for the following parameters: $\lambda = 355\,\text{nm}$, $h_0 = 68.5\,\text{mm}$, $h_g = 2\,\text{nm}$, $w_g = 1\,\text{mm}$, $\alpha = 4.77\,\mu\text{rad}$.

It can be seen that the ray-optics approximation gives
55 a "zigzag" pattern, whereas the correct structure has more "broken" appearance, with the fringe divided into separate segments. This broken structure was found to be in better agreement with experimental data for this type of plate defect.

In addition to better describing the effects of plate defects,
60 the wave-optics approach allows for a natural treatment of the range of incidence angles present in a lidar system by treating the input radiation as a Gaussian speckle pattern. This is described in detail in Sect. A3. Wave-optics also allows the modelling of diffraction effects due to intensity vari-
65 ation in the input light, e.g. arising from obscuration. Section A4 briefly outlines an alternative approach to including a range of incidence angles, still based on the wave-optic model but using an incoherent sum of plane-wave components.
70

A1 Modelling approach

The geometry of the Fizeau is sketched in Fig. 1, in the schematic of the Mie channel. Note that the wedge angle, α, is greatly exaggerated: in the instrument under consideration, α is just $4.77\,\mu\text{rad}$, as listed in Table 1.
75 For a given input field E_I we wish to calculate the output field E_O and the output intensity $I_\text{O} = |E_\text{O}|^2$. Let E_1 be the field transmitted through the second plate after the light has undergone one pass of the Fizeau. This is given by

$E_1 = t_A F\{E_\text{I}\} t_B,$ (A3)
80

where t_A and t_B are the amplitude transmission coefficients of the plates A and B, and F is an operator that takes the field after the first plate and transforms it to the field before the second plate. For simplicity, the plates are taken to have
85 zero thickness. The transmitted field after the light has made a further round trip through the Fizeau is given by

$E_2 = r_B r_A F^2\{E_1 \exp(2\,i\,k\,\alpha\,x)\}.$ (A4)

Here, it is the second plate, B, that is angled with respect to the x direction, with plate A parallel to x. Owing to the small size of the angle, the effect of the wedge is simply a phase
90 shift on the reflected radiation that is proportional to α and x. k is the wave vector of the incident field, and r_A and r_B are the amplitude reflection coefficients of the plates. Since the reverse passage $B \rightarrow A$ is determined by the same operator as the passage $A \rightarrow B$, we use the notation F^2 for the dou-
95 ble application of the operator F. Note that the transmission
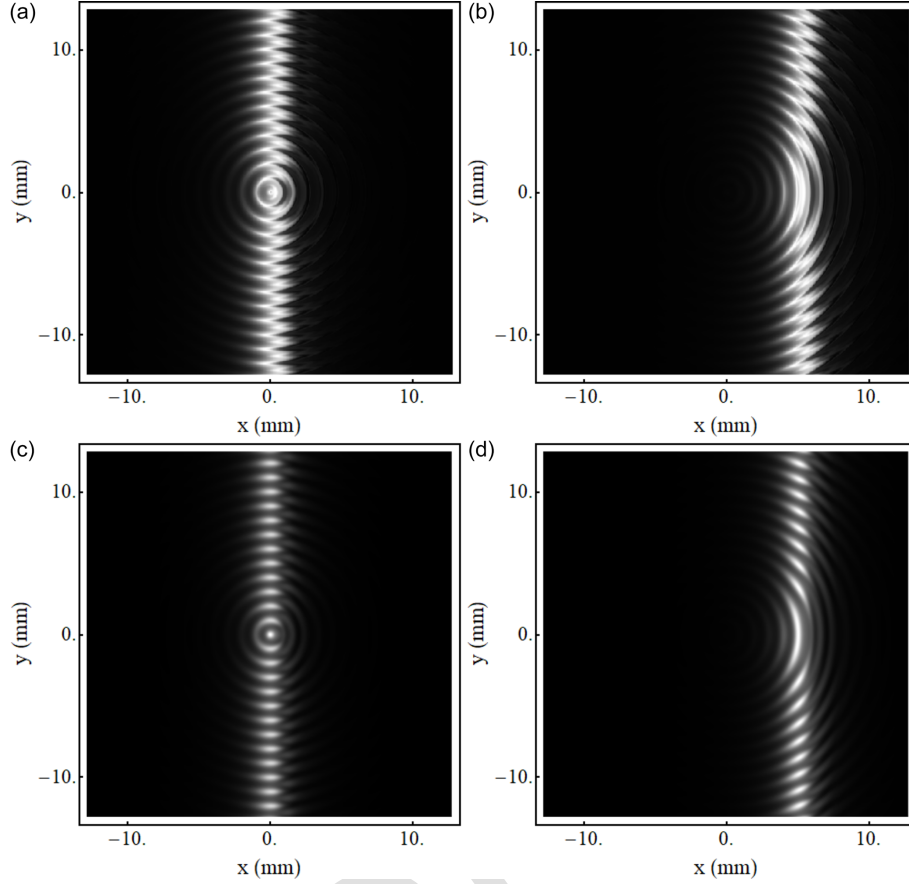
Figure A1. Four modelled fringe patterns in the presence of circular plate defects. Panels **(a)** and **(b)** show ray-optic modelling, using two slightly different wavelengths to give a different fringe location in each figure. Panels **(c)** and **(d)** are the corresponding wave-optics results.

factor t_B does not need to be applied again as it is already included in E_1 (see Eq. A3). Equation (A4) can be extended to the $n + 1$th pass through the Fizeau as follows:

$$E_{n+1} = r_B \, r_A \, F^2 \{ E_n \exp (2 \, i \, k \, \alpha \, x) \}. \tag{A5}$$

Finally, one can write

$$E_O = \sum_{n=1}^{N} E_n. \tag{A6}$$

The value of N is chosen to be sufficiently large that inclusion of further passages through the Fizeau has a negligible effect on the resulting fringe profile. The appropriate value of N will depend on the plate reflectivities. For example, with both plates having the same intensity reflection coefficients of $R = 0.88$, $N = 55$ is found to give satisfactory results. An order-of-magnitude estimate of the terms being neglected can be found by noting that, after N round trips, the neglected fractional power inside the Fizeau is of order R^{2N}, which is 3.6×10^{-5} in this case.

A2 Solution of paraxial wave equation

The operator F introduced in Sect. A1 is implemented by starting with the paraxial wave equation for monochromatic radiation in Cartesian coordinates, which is

$$\frac{\partial^2 E}{\partial x^2} + \frac{\partial^2 E}{\partial y^2} - 2 \, i \, k \frac{\partial E}{\partial z} = 0, \tag{A7}$$

where the wave is propagating in the z direction, taken to be the direction normal to the first plate. Equation (A7) is solved using a Fourier-domain approach. Fourier transformation with respect to the x and y coordinates is applied to the equation. The resulting ordinary differential equation in z has the following solution:

$$\overline{E}(\boldsymbol{\omega}, z_B) = \overline{E}(\boldsymbol{\omega}, z_A) \exp \left[\frac{i |\boldsymbol{\omega}|^2 (z_B - z_A)}{2k} \right]. \tag{A8}$$

Here, $\boldsymbol{\omega}$ is the spatial frequency vector, $\overline{E}(\boldsymbol{\omega}, z_A)$ is the Fourier transform of the known field in the z_A plane, and $\overline{E}(\boldsymbol{\omega}, z_B)$ is the transform of the desired field in the z_B plane. The field itself is produced via the inverse transform. The
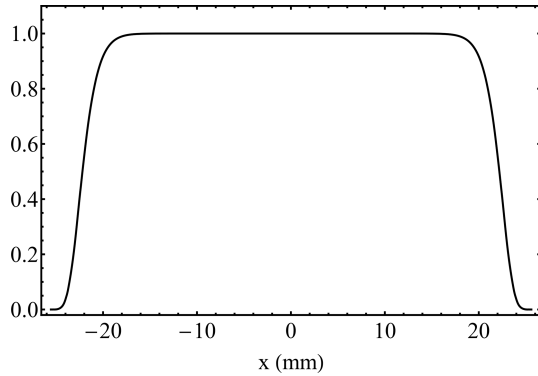
Figure A2. Tapered input profile.

Figure A3. Fringe produced using increasing numbers of round trips for a tilt angle of 300 µrad. Cyan is $N = 14$, red is $N = 28$, and black is $N = 55$.

Fourier transforms are calculated using the fast Fourier transform (FFT) algorithm; more details can be found in Jakeman and Ridley (2006). The input field is defined on a discrete grid. A square grid is used here, but a rectangular grid is also possible. Typically, the grid consists of 1024 by 1024 points, with a space step size of 50 µrad. One potential issue with the FFT method is that it is periodic in space, which can lead to edge effects. This is avoided by, first, making sure that the Fizeau fringe appears near the centre of the grid, via precise setting of the wavelength, and, second, tapering the input intensity to zero at the edges of the input wave. This tapering uses a super-Gaussian profile of 10th order, i.e. $\exp\left(-|r/w_s|^{20}\right)$, where r is a 2D position vector with origin at the centre of the grid, and the super-Gaussian radius is $w_s = 23.4$ mm. It is worth mentioning that the tapering does not effect the region of interest, which is the 36 mm Fizeau diameter. A cross-section through this tapered profile is shown in Fig. A2.

It would also be possible to use a profile similar to that in Fig. A2 as an absorbing boundary applied to one of the mirrors. However, it was found that tapering of the input wave amplitude worked well enough. Figure A3 shows example Fizeau fringes using three different values of $N = 14$ (cyan), $N = 28$ (red), and $N = 55$ (black). The Fizeau parameters used for simulation are a plate separation of 68.5 mm, a wedge angle of 4.77 µrad, reflectivity $R = 0.88$, and a wavelength of 355 nm. The free spectral range is $\lambda/2\alpha = 37$ mm and the length of the modelled region is 51.2 mm. Thus, with the fringe at the centre of the region, the fringe corresponding to the adjacent FSR is well away from the edge, reducing the possibility of spurious diffraction at the edge contaminating the central fringe profile. Here, the incident field is a plane wave with a tilt angle of 300 µrad relative to the z axis (i.e. the normal of plate A). The convention used here is that positive angles tilt the input radiation in the direction of increasing plate separation (i.e. increasing because of the wedge).

Here, the intensity is normalized by the input intensity. As mentioned previously, a value of $N = 55$ was considered suf-
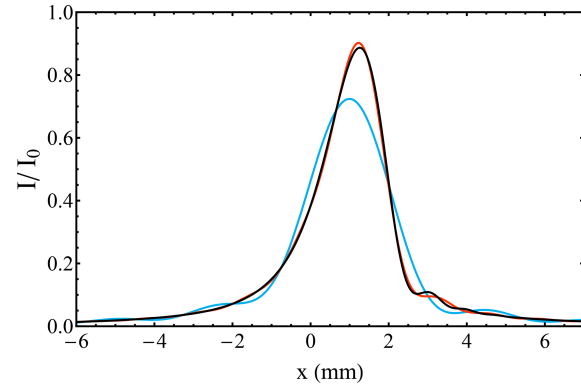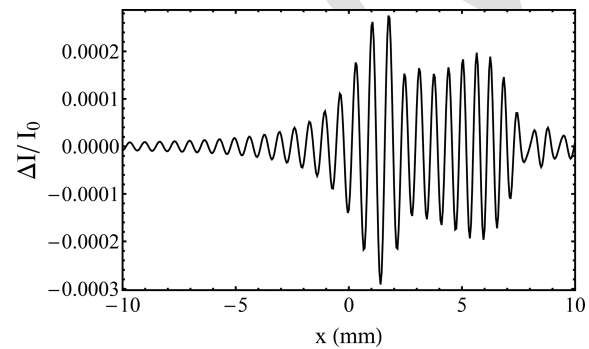
Figure A4. Relative differences in intensities for 55 loops versus 100 loops.

ficient for this work. A further indication of the errors involved in truncating the summation in Eq. (A4) is given in Fig. A4, which shows the difference in intensity of fringes produced with $N = 55$ and $N = 100$. It can be seen that the maximum difference is of order 2×10^{-4}, relative to the input intensity. Note that this is nearly an order of magnitude greater than the estimate in the previous section, based on total power. This discrepancy can be explained by the fact that the intensity differences are both positive and negative, so there is significant cancellation when a difference in power is considered because the power is a spatial integration of intensity.

Note that, in this case, the ray-optics approach of Eq. (A1) gives an almost identical fringe profile, so this particular scenario of plane-wave illumination and perfect plates does not necessitate a wave-optics approach.

A3 Coherence and averaging

In practice, in a pulsed Doppler wind lidar, the radiation incident on the Fizeau will not be a coherent plane wave. Therefore, the Fizeau model needs to take into account the actual structure of the input radiation. At any given moment in time,

the laser illuminates a large number of scatterers within a volume determined by the spatial extent of the laser beam and its pulse duration. As a result, the field incident on the Fizeau interferometer will be a Gaussian speckle pattern. During the time corresponding to the range gate of the system, the pulse will illuminate different sets of scatterers, and the accumulated fringe will be temporally averaged, which smooths out the speckle variations. In addition, there will be further smoothing when fringes from multiple pulses are summed. In the Aeolus spectrometer, spatial averaging also occurs because the detector readout is summed along the length of the fringe. It is worth reviewing and quantifying these various averaging/smoothing effects.

Consider a monostatic system, with the transmit–receive telescope producing a plane-wave input to the Fizeau interferometer from any individual (far-field) scatterer.

Consider, first, a single scattering layer situated at range $z = L$. For simplicity, we take $z = 0$ as being the position of the telescope entrance pupil. Assume the laser beam illuminating the scattering layer is a TEM_{00} Gaussian; it has an intensity profile given by

$$I(r) = I_0 \exp\left(-2\frac{r^2}{w^2(z)}\right). \tag{A9}$$

The beam radius at the $1/e^2$ intensity point is

$$w^2(z) = w_0^2\left[1 + \left(\frac{2z}{k\,w_0^2},\right)^2\right]. \tag{A10}$$

The backscattered light at the telescope pupil will form a speckle pattern. It can be shown that this speckle pattern will be characterized by a field correlation function of the form (Jakeman and Ridley, 2006)

$$\left|g^{(1)}(r)\right| = \exp\left[-\frac{1}{2}\left(\frac{k\,w(L)\,r}{2\,L}\right)^2\right], \tag{A11}$$

with r being the distance between any two points in the $z = 0$ plane. Note that this is the modulus of the correlation function. The full, complex correlation function includes a phase term associated with the curvature of the wavefront returning from the scattering layer. However, because we have assumed a telescope focused on the scattering layer, this phase term is removed by the telescope and does not apply to the speckle pattern entering the Fizeau interferometer. Thus, in the numerical modelling of speckles, there is no phase term, and the auto-correlation function is real rather than complex. Employing the Siegert relation (Jakeman and Ridley, 2006), the intensity correlation function can be shown to be

$$g^{(2)}(r) = 1 + \exp\left[-\left(\frac{k\,w(L)\,r}{2\,L}\right)^2\right]. \tag{A12}$$

The speckle size can be characterized by a single correlation length, defined as the separation r at which the exponential
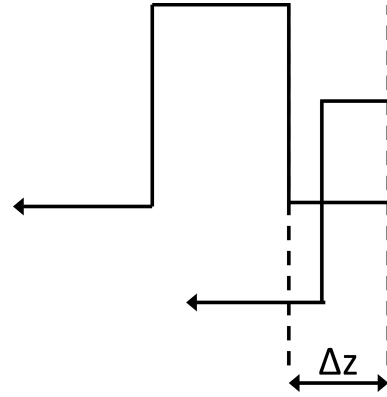
Figure A5. Backscatter from two separate layers.

term in Eq. (A12) has reduced by $1/e$. When the scattering layer is in the far field, the correlation length is simply

$$r_{\frac{1}{e}} = \frac{\lambda}{\pi\theta_b}, \tag{A13}$$

where $w(L) = \theta_b L$. The beam divergence half angle θ_b is

$$\theta_b = \frac{\lambda}{\pi\,w_0}. \tag{A14}$$

In a monostatic lidar, the system field of view is determined by the divergence of the illuminating beam and, in one dimension, is $2\theta_b$.

We can define a correlation area as

$$A_c = \pi\,r_{\frac{1}{e}}^2. \tag{A15}$$

If the telescope has the magnification M, then the angular factors at the input to the Fizeau interferometer will increase by M, and the length scales decrease by M. Thus, the field input to the interferometer is also a speckle pattern, with a correlation length reduced by a factor of M. The output of the interferometer will also be a speckle pattern but with more complicated correlation properties. Roughly speaking, it can be considered to be an interference fringe modulated by a random speckle pattern. When averaged over many independent random speckle patterns, a smoothed fringe will emerge, the width of the fringes being influenced by the correlation length of the original speckle pattern (or, equivalently, the lidar FOV): a larger FOV means a shorter correlation length (via Eq. A13), which will result in a broader fringe.

Consider, first, the significance of the laser pulse duration. Figure A5 shows a simplified situation where there are only two scattering layers at different distances from the instrument.

Let the laser pulse duration be τ, with the second scattering layer separated from the first by a distance Δz, which is greater than $\tau c/2$. It is evident that the leading edge of the pulse reflected from the second layer cannot overlap the

trailing edge of the pulse reflected from the first. Thus, at the entrance to the spectrometer, there would be a certain speckle pattern for a period of time τ followed by a second, independent speckle pattern, also of duration τ. In the more general case, where scatterers are uniformly distributed along the beam propagation path, the speckle pattern will vary continuously in time, with a characteristic time constant of τ. Provided the time taken for light to propagate through the interferometer is significantly shorter than the pulse duration, the same characteristic time constant τ applies to the output of the Fizeau interferometer. The temporal averaging is achieved simply by accumulating light on the detector for a time duration longer than the speckle correlation time. The number of averages can be taken to be the ratio of this detector time gate to the speckle correlation time. In terms of the vertical spatial resolution of the wind measurement, R_v, the number of speckles averaged, is simply

$$N_1 = \frac{2R_\mathrm{v}}{\tau c}. \tag{A16}$$

Note that this assumes that the scattering cross-section is uniform along the length of the volume being probed by the laser beam. If the scattering cross-section is non-uniform, different scattering layers will reflect different quantities of laser light, and the effective number of averages will be less than the result of Eq. (A16). In addition, Eq. (A16) assumes that the pulse is fully temporally coherent. If this is not the case, the pulse duration τ must be replaced by the (shorter) coherence time. The spatial averaging is carried out after the speckle light has been detected: columns of pixels are summed along the direction of the fringe. The number of effective averages here depends on the size of the speckle and the size of the detector pixels. Using Eq. (A13) with $\theta_b = 6\,\mu\mathrm{rad}$ and 355 nm wavelength gives a speckle size of 1.9 cm at the entrance to the telescope and thus a speckle area of 11.3 cm^2. Dividing by the telescope magnification $M = 41.7$ gives a speckle size of 0.45 mm at the entrance to the interferometer. Equation (A13) thus gives a speckle area at the entrance to the interferometer of 0.64 mm^2. Assume that there is the same number of speckles at the output of the interferometer and that the speckle size is the same across every column of pixels; i.e. it does not vary at different positions in the fringe pattern. Now, each detector pixel is a square of 1.6 mm width, and there are 16 pixels in a column. Thus, when the speckle pattern is averaged over a column, there are approximately $N_2 = 41/0.64 = 64$ effective speckles averaged over. In fact, taking the effective number of speckles as the detector area divided by the speckle area is only exact in the limit of a large number of speckles. For a square detector area, the exact result for the effective number of speckles is (Goodman, 2007)

$$N_2 = \left(\frac{1}{\sqrt{a}} Erf\left[\sqrt{\pi a} - 1\right] - \frac{1}{\pi a}\left[1 - \exp(-\pi a)\right] \right)^{-2}, \tag{A17}$$

where a is the detector area divided by the speckle area. This formula gives $N_2 = 69.4$ as the effective number of speckles. Note, however, that this is still an approximation because the detector column is rectangular rather than square.

The third stage of averaging comes from accumulation of signal from multiple, independent pulses. If the number of pulses averaged is N_3, we can define a total number of effective averages as

$$N_T = N_1 N_2 N_3. \tag{A18}$$

Now, the statistics of an individual speckle pattern are negative exponential in form (Jakeman and Ridley, 2006):

$$P(I) = \frac{1}{I_\mathrm{A}} \exp\left(-\frac{I}{I_\mathrm{A}}\right), \tag{A19}$$

where I_A is the average intensity. Note that when we consider the output of the interferometer, the average intensity is spatially varying: high near the peak of a fringe and low in the troughs. The sum of N speckle patterns follows a gamma distribution (Jakeman and Ridley, 2006):

$$P(I) = \frac{I^{N-1}}{I_A^N \Gamma(N)} \exp\left(-\frac{I}{I_\mathrm{A}}\right), \tag{A20}$$

where Γ is the Euler gamma function. This result can also be used when N is not an integer. The average intensity is $N I_\mathrm{A}$. The degree of fluctuation can be characterized by the second moment

$$\frac{\langle I^2 \rangle}{\langle I \rangle^2} = 1 + \frac{1}{N}. \tag{A21}$$

Clearly, this takes on the value of 2 when there is no averaging and reduces to unity as $N \to \infty$. In the large N limit, the detector output, in the absence of other noise sources, can be considered a sum of a constant term and a smaller fluctuating term, which varies from measurement to measurement. Thus, in this large N limit, one can define an effective signal-to-noise ratio (SNR) as the constant term divided by the standard deviation of the fluctuating term. Using Eq. (A21), it is simple to show that this SNR is just $\sqrt{N_T}$. As stated above, we have $N_2 = 69.4$. The minimum range gate is 2.1 μs and the pulse duration 20 ns, which gives $N_1 = 110$. Thus, even without considering multiple pulse averaging, the minimum speckle SNR in normal operation is 87, which is sufficiently high to make this a small noise component compared to shot noise on the Rayleigh background. The number of laser pulses P averaged on the CCD is $P - 1$, and afterwards, $N \cdot (P - 1)$ is averaged to one observation. P has changed in the course of the mission, and respective values are available in the ACCD paper by Lux et al. (2024). The effect of speckle smoothing/averaging is included in the wave-optic model by calculating multiple fringes, each starting with a statistically independent speckle pattern and averaging the fringes to produce the final, smoothed, fringe.
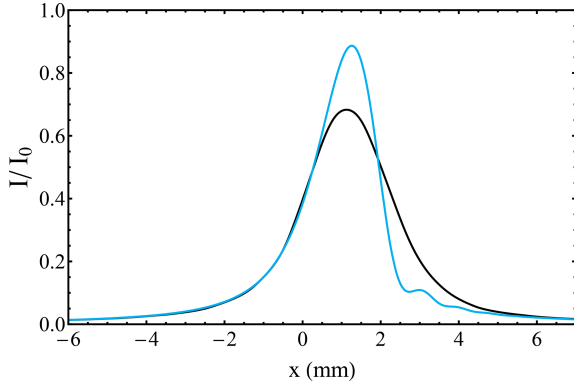
Figure A6. Fringe with a Gaussian angular spectrum (black) compared with a plane wave (cyan). The other parameters are the same as in Fig. A3.

Typically, 100 different speckle patterns were used for each fringe. Note that it is not necessary to match the number of averages given by Eq. (A18): it is sufficient to use enough averages that residual speckle noise is negligible. Details
5 of the generation of random speckle patterns can be found in Jakeman and Ridley (2006). The basis is the expression given by Eq. (A11) for the field correlation function. The Fourier transform of this is multiplied by an array of delta-correlated random complex Gaussian-distributed noise val-
10 ues. Inverse transformation yields two independent speckle patterns from the real and imaginary components. An example of a speckle-averaged fringe is shown in Fig. A6, compared with the plane-wave fringe of Fig. A3. This uses the same central tilt angle of 300 µrad but with a Gaussian angu-
15 lar spectrum of $1/e$ width of 500 µrad.

Here, the two fringes have the same power, i.e. equal area under the fringe. Significant broadening of the fringe can be seen, as well as the influence of the Fizeau fringe asymmetry. It is worth noting that the broadened profile cannot simply be
20 considered a convolution of the plane-wave fringe with the angular spectrum because the shape of the plane-wave fringe is itself strongly dependent on the AOI.

This result used 100 speckle averages. An idea of the magnitude of the errors (i.e. the "speckle noise") in this case can
25 be found by calculating a second fringe with independent random speckles. The result of differencing the intensity of the two fringes is given in Fig. A7. Noting that one expects a square-root-of-2 increase in errors when differencing two random quantities, it can be inferred that the maximum in-
30 tensity error is of order 2 %.

A4 Angular spectrum approach

The speckle approach described above treats the physics without any major approximations, but it does have the disadvantage of requiring averaging over many independent ran-
35 dom speckle patterns to get an acceptably low error, which
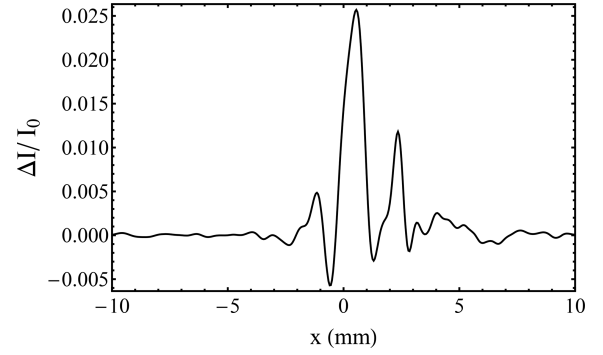
Figure A7. Residual errors from speckle fringe calculation from two independent simulations with $N = 100$ speckles.
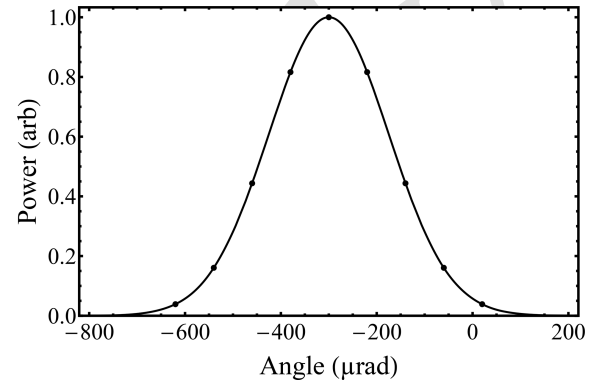
Figure A8. Angular spectrum approach to fringe calculation.

has implications for the time taken to compute a single fringe. If one is only interested in the incoherent fringe that results in the limit of infinite averaging, there is an alternative approach. This involves calculating many plane-wave fringes for different angles of incidence and combining them 40 by adding intensities rather than fields. A far-field illuminating laser profile, such as that given by Eq. (A9), can be converted into an angular spectrum, here denoted $\mathcal{A}$. This is the field angular spectrum, so the amplitude of $\mathcal{A}$ is the square root of the laser intensity at a given angle. If we consider 45 the backscatter to come from a continuous scattering layer, the field at the input to the Fizeau can be written as a two-dimensional integral over the vector angle $\boldsymbol{\nu}$:

$$\int \mathcal{A}(\boldsymbol{\nu}) \exp(i\,k\,\boldsymbol{\nu}\,r)\,\mathrm{d}\boldsymbol{\nu}. \tag{A22}$$

The field at the output of the Fizeau can similarly be written 50 as an integral over an angle-dependent transmission function f (not to be confused with the earlier operator F as introduced in Eq. A5):

$$E_{\mathrm{O}} = \int \mathcal{A}(\boldsymbol{\nu}) f(\boldsymbol{\nu})\mathrm{d}\boldsymbol{\nu}. \tag{A23}$$

Note that, here, the exponential phase factor in Eq. (A22) 55 has been subsumed into f. Treating the scattering amplitude

as a random variable (i.e. constant amplitude and random phase, the random phase arising from the random positioning of the scatterers), the incoherent fringe intensity can be written as an ensemble average, indicated by angled brackets in Eq. (A24). TS1

$$I_O = \langle |E_O|^2 \rangle = \int \int \langle \mathcal{A}(\boldsymbol{\nu})\mathcal{A}(\boldsymbol{\nu}') \rangle f(\boldsymbol{\nu}) f(\boldsymbol{\nu}') \mathrm{d}\boldsymbol{\nu}\mathrm{d}\boldsymbol{\nu}' \quad \text{(A24)}$$

When the average is taken, only the radiation from individual scattering centres (e.g. single angles of arrival) combines constructively because the complex quantities $\mathcal{A}(\boldsymbol{\nu})$ and $\mathcal{A}(\boldsymbol{\nu}')$ have the same phases when $\boldsymbol{\nu} = \boldsymbol{\nu}'$. Cross-terms between different scattering centres are randomly phased and average zero. This means the correlation function can be written as a delta function with respect to the angle

$$\langle \mathcal{A}(\boldsymbol{\nu})\mathcal{A}(\boldsymbol{\nu}') \rangle = |\mathcal{A}(\boldsymbol{\nu})|^2 \delta(\boldsymbol{\nu} - \boldsymbol{\nu}'). \quad \text{(A25)}$$

Substituting Eq. (A25) into Eq. (A24) results in the removal of one of the integrals, giving

$$I_O = \int |\mathcal{A}(\boldsymbol{\nu})|^2 |f(\boldsymbol{\nu})|^2 \mathrm{d}\boldsymbol{\nu}. \quad \text{(A26)}$$

That is, the fringe profile is a weighted integral over a set of plane-wave fringes. For numerical calculations, the integral is replaced by a sum over a suitably chosen set of angles. In the results given here, the appropriate number of angles to use was determined by comparing fringes with a different number of angles and also by comparing with the speckle approach. It was found that 81 angles in a 9 by 9 regularly spaced (square) array, with an angular spacing of 80 µrad, were acceptable for calculating a fringe using the parameters of Fig. A6. A cross-section through the centre of this array is shown in Fig. A8, where the solid line shows the Gaussian angular spectrum and the discrete points the angles used for each plane-wave calculation.

Figures A9 and A10 show differences between the 9 by 9 array and a result with 13 by 13 angles and the 100 speckle average result of Fig. A6, respectively.

Figure A10. Differences between a fringe calculated with 9 by 9 angles and one using the speckle approach with 100 speckle averages.

These results imply that the angular spectrum is accurate with 81 angles. In fact, Fig. A10 suggests it is more accurate than the speckle result, with 100 speckles, because the differences are of similar magnitude to those seen in Fig. A7, meaning that errors in the speckle approach are larger.

In terms of computation time, the angular spectrum approach is somewhat faster than the speckle approach in this case because it uses 81 fringe calculations rather than 100 and because it does not require additional time to generate the random speckle patterns. However, the real computational advantage would come in cases where one needs to compute full two-dimensional fringes, without the averaging over detector columns. It was shown earlier in the discussion following Eq. (A16) that this averaging is equivalent to 64 speckle averages. So, if this additional averaging was not employed, 64 times more independent speckle patterns would need to be used, with a proportional increase in computation time.

Figure A9. Differences between a fringe calculated with 9 by 9 angles and one with 13 by 13 angles.

Appendix B: Nomenclature

Γ_{FSR}	Free spectral range
$\mathcal{P}_{\text{Raw}}$	Raw signal fringe profile
$\mathcal{P}_{\text{Las}}$	Laser pulse profile
$\mathcal{P}_{\text{Fiz}}$	Fizeau instrument profile
$\mathcal{P}_{\text{Det}}$	Detector channel spectral profile
$\mathcal{L}(x)$	Lorentzian peak function
$\mathcal{I}_{\mathcal{L}}$	Area under $\mathcal{L}(x)$
$\Gamma_{\mathcal{L}}$	Full width at half maximum of $\mathcal{L}(x)$
x_0	Centre position
Γ_{TH}	Width of top-hat function
$H(x)$	Heaviside step function
$\mathcal{L}_{\text{px}}(x)$	Pixelated Lorentzian profile
$\mathcal{I}_{\mathcal{L}_{\text{px}}}$	Area under $\mathcal{L}_{\text{px}}(x)$
$\mathcal{V}(x)$	Voigt peak function
$\Gamma_{\mathcal{V}}$	Full width at half maximum of $\mathcal{V}(x)$
$\mathcal{G}(x)$	Gaussian peak function
$\Gamma_{\mathcal{G}}$	Full width at half maximum of $\mathcal{G}(x)$
$\mathcal{I}_{\text{fringe}}$	Total fringe intensity
$\mathcal{I}_{\text{peak}}$	Fringe peak intensity
$\mathcal{L}_{\text{fraction}}$	Fractional Lorentzian contribution to $\mathcal{V}(x)$
$\mathcal{G}_{\text{fraction}}$	Fractional Gaussian contribution to $\mathcal{V}(x)$
p	Numerical value from Voigt tables
L_{FWHM}	Lorentzian FWHM contribution to $\Gamma_{\mathcal{V}}$
G_{FWHM}	Gaussian FWHM contribution to $\Gamma_{\mathcal{V}}$
R	Reflectivity
T	Transmission
F	Finesse coefficient
φ	Phase lag
$\mathcal{A}(\varphi)$	Airy function
N_{R}	Reflectivity finesse
$\Delta\tau$	Laser pulse duration
$\Delta\nu$	Fourier-transform limit of laser spectral width
δf	Standard deviation of frequency estimates
C	Spectral shape constant
$C_{\mathcal{L}}$	Spectral shape constant for $\mathcal{L}(x)$
$C_{\mathcal{G}}$	Spectral shape constant for $\mathcal{G}(x)$
$C_{\mathcal{V}}$	Spectral shape constant for $\mathcal{V}(x)$
$\langle N_S \rangle$	Mean number of electron counts
SNR	Signal-to-noise ratio in shot noise limit
$\text{SNR}_{\text{basic}}$	Basic SNR calculation with background present
m	Total number of detector pixels
$\text{SNR}_{\text{refined}}$	Refined SNR calculation with background present
N_{ped}	Background signal per pixel
k_{r}	Signal fraction within the analytical bandwidth
f_{AB}	Analytical bandwidth
n	Number of pixels covered by f_{AB}
r	Ratio of f_{AB} and δf
δv_{HLOS}	Standard deviation of the HLOS wind

Code availability. The code that is used for data analysis (Lab-VIEW vi) and for figure plotting (OriginLab) can be provided upon request.

Data availability. The particular data sets used in this study can be provided upon request.

Author contributions. MV led the presented study, which already started back in 2013, and performed the main part of the presented analysis. KR developed the wave-optic model for the Fizeau spectrometer and performed all the corresponding simulations. BW performed the numerical simulations and supported the preparation of the manuscript. OL provided the data of the Aeolus Fizeau fringes and supported the corresponding analysis. IN generated the Aeolus prototype fringes and supported the corresponding analysis. OR supported the data analysis and the preparation of the paper.

Competing interests. The contact author has declared that none of the authors has any competing interests.

ther geographical representation in this paper. While Copernicus Publications makes every effort to include appropriate place names, the final responsibility lies with the authors.

Acknowledgements. With the greatest respect and appreciation, the authors offer tribute to the memory of Alain Culoma (ESA), for his far-sighted and enthusiastic support for the development of wave-optic modelling techniques. The authors also would like to thank Eric Jakeman for helpful discussions during the development of the wave-optic model and Christian Lemmerz for his contributions during the investigations discussed in this paper.

Financial support. This research has been supported by the European Space Agency (grant nos. 5401001330, 5401002470, 40000126336/18/I-BG, and 4000144330/24/I-AG).

The article processing charges for this open-access publication were covered by the German Aerospace Center (DLR).

Review statement. This paper was edited by Ad Stoffelen and reviewed by two anonymous referees.

References

Baars, H., Herzog, A., Heese, B., Ohneiser, K., Hanbuch, K., Hofer, J., Yin, Z., Engelmann, R., and Wandinger, U.: Validation of Aeolus wind products above the Atlantic Ocean, At-

mos. Meas. Tech., 13, 6007–6024, https://doi.org/10.5194/amt-13-6007-2020, 2020.

Baker, W. E., Atlas, R., Cardinali, C., Clement, A., Emmitt, G. D., Gentry, B. M., Hardesty, R. M., Källén, E., Kavaya, M. J., Langland, R., Ma, Z., Masutani, M., McCarty, W., Pierce, R. B., Pu, Z., Riishojgaard, L. P., Ryan, J., Tucker, S., Weissmann, M., and Yoe, J. G.: Lidar-Measured Wind Profiles: The Missing Link in the Global Observing System, B. Am. Meteor. Soc., 95, 543–564, https://doi.org/10.1175/BAMS-D-12-00164.1, 2014.

Born, M. and Wolf, E.: Principles of optics: electromagnetic theory of propagation, interference and diffraction of light, Pergamon, Oxford, England, https://doi.org/10.1175/BAMS-D-12-00164.1, 1980.

Borne, M., Knippertz, P., Weissmann, M., Witschas, B., Flamant, C., Rios-Berrios, R., and Veals, P.: Validation of Aeolus L2B products over the tropical Atlantic using radiosondes, Atmos. Meas. Tech., 17, 561–581, https://doi.org/10.5194/amt-17-561-2024, 2024.

Brossel, J.: Multiple-beam localized fringes: Part I. Intensity distribution and localization, P. Phys. Soc., 59, 224–234, https://doi.org/10.1088/0959-5309/59/2/306, 1947.

Chanin, M., Garnier, A., Hauchecorne, A., and Porteneuve, J.: A Doppler lidar for measuring winds in the middle atmosphere, Geophys. Res. Lett., 16, 1273–1276, 1989.

Cosentino, A., D'Ottavi, A., Sapia, A., and Suetta, E.: Space-borne lasers development for ALADIN and ATLID instruments, in: 2012 IEEE International Geoscience and Remote Sensing Symposium, 22–27 July 2012, Munich, Germany, 5673–5676, https://doi.org/10.1109/IGARSS.2012.6352324, 2012.

Cosentino, A., Mondello, A., Sapia, A., D'Ottavi, A., Brotini, M., Nava, E., Stucchi, E., Trespidi, F., Mariottini, C., Wazen, P., Falletto, N., and Fruit, M.: High energy, single frequency, tunable laser source operating in burst mode for space based lidar applications, in: International Conference on Space Optics – ICSO 2004, edited by: Costeraste, J. and Armandillo, E., International Society for Optics and Photonics, SPIE, 30 March–2 April 2004, Toulouse, France, 10568, 1056817, https://doi.org/10.1117/12.2308024, 2017.

Durand, Y., Meynart, R., Culoma, A., Morancais, D., and Fabre, F.: Results of the pre-development of ALADIN, the direct detection Doppler wind lidar for ADM/Aeolus, in: Sensors, Systems, and Next-Generation Satellites VIII, 5570, 93–104, SPIE, 2004.

ESA: The four candidate Earth explorer core missions: Atmospheric dynamics mission, ESA Report for Mission Selection ESA SP-, 1233, 145 pp., ISBN 92-9092-528-0, 1999.

ESA: ADM-Aeolus, Science Report, ESA-SP-1311, ISBN 978-92-9221-404-3, 2008.

ESA: ADM-Aeolus Mission Requirements Documents, AE-RP-ESA-SY-001, 2016.

Flesia, C. and Korb, C.: Theory of the double-edge molecular technique for Doppler lidar wind measurement, Appl. Opt., 38, 432–440, 1999.

Francou, L., Grond, E. R., Blum, S., and Voland, C.: Optical analysis and performance verification on ALADIN spectrometers, in: International Conference on Space Optics – ICSO 2008, Toulouse, France, 14–17 October 2008, 10566, 518–523, SPIE, https://doi.org/10.1117/12.2308260, 2017.

Gentry, B. M., Chen, H., and Li, S. X.: Wind measurements with 355-nm molecular Doppler lidar, Opt. Lett., 25, 1231–1233, 2000.

Goodman, J. W.: Speckle phenomena in optics: theory and applications, Roberts and Company Publishers, ISBN 0-9747077-9-1, 2007.

Harris, D. C.: History of magnetorheological finishing, in: Window and dome technologies and materials XII, 8016, 206–227, SPIE, 2011.

Hernandez, G.: Fabry-Perot Interferometers, Cambridge University Press, ISBN 0 521 32238 3, 1986.

Horányi, A., Cardinali, C., Rennie, M., and Isaksen, L.: The assimilation of horizontal line-of-sight wind information into the ECMWF data assimilation and forecasting system. Part I: The assessment of wind impact, Q. J. Roy. Meteor. Soc., 141, 1223–1232, 2015.

Jacobs, S. D., Golini, D., Hsu, Y., Puchebner, B. E., Strafford, D., Prokhorov, I. V., Fess, E. M., Pietrowski, D., and Kordonski, W. I.: Magnetorheological finishing: a deterministic process for optics manufacturing, in: International Conference on Optical Fabrication and Testing, Tokyo, Japan, 2 August 1995, 2576, 372–382, SPIE, https://doi.org/10.1117/12.215617, 1995.

Jakeman, E. and Ridley, K. D.: Modeling fluctuations in scattered waves, CRC Press, https://doi.org/10.1201/9781420012163, 2006.

Kajava, T., Lauranto, H., and Salomaa, R.: Fizeau interferometer in spectral measurements, JOSA B, 10, 1980–1989, 1993.

Kanitz, T., Lochard, J., Marshall, J., McGoldrick, P., Lecrenier, O., Bravetti, P., Reitebuch, O., Rennie, M., Wernham, D., and Elfving, A.: Aeolus first light: first glimpse, in: International Conference on Space Optics – ICSO 2018, Chania, Greece, 12 July 2019, 11180, 111801R, International Society for Optics and Photonics, https://doi.org/10.1117/12.2535982, 2019.

Koechner, W.: Solid-state laser engineering, vol. 1, Springer, https://doi.org/10.1007/978-3-662-15143-3, 2013.

Langenbeck, P.: Fizeau interferometer–fringe sharpening, Appl. Opt., 9, 2053–2058, 1970.

Lux, O., Lemmerz, C., Weiler, F., Marksteiner, U., Witschas, B., Rahm, S., Geiß, A., and Reitebuch, O.: Intercomparison of wind observations from the European Space Agency's Aeolus satellite mission and the ALADIN Airborne Demonstrator, Atmos. Meas. Tech., 13, 2075–2097, https://doi.org/10.5194/amt-13-2075-2020, 2020.

Lux, O., Lemmerz, C., Weiler, F., Kanitz, T., Wernham, D., Rodrigues, G., Hyslop, A., Lecrenier, O., McGoldrick, P., Fabre, F., Bravetti, P., Parrinello, T., and Reitebuch, O.: ALADIN laser frequency stability and its impact on the Aeolus wind error, Atmos. Meas. Tech., 14, 6305–6333, https://doi.org/10.5194/amt-14-6305-2021, 2021.

Lux, O., Lemmerz, C., Weiler, F., Marksteiner, U., Witschas, B., Rahm, S., Geiß, A., Schäfler, A., and Reitebuch, O.: Retrieval improvements for the ALADIN Airborne Demonstrator in support of the Aeolus wind product validation, Atmos. Meas. Tech., 15, 1303–1331, https://doi.org/10.5194/amt-15-1303-2022, 2022.

Lux, O., Reichert, R., Lemmerz, C., Masoumzadeh, N., Wernham, D., Candra Krisna, T., Marchais, D., Bell, R., Parrinello, T., and Reitebuch, O.: CCD detector performance of the space-borne Doppler wind lidar ALADIN during the Aeolus mission, Appl. Opt., 63, 6754–6775, 2024.

Marksteiner, U., Lemmerz, C., Lux, O., Rahm, S., Schäfler, A., Witschas, B., and Reitebuch, O.: Calibrations and Wind Observations of an Airborne Direct-Detection Wind LiDAR Supporting ESA's Aeolus Mission, Remote Sens., 10, 2056, https://doi.org/10.3390/rs10122056, 2018.

Marksteiner, U., Lux, O., Reitebuch, O., de Kloe, J., Marseille, G.-J., and Rennie, M.: Overview of Instrument Response Calibrations, in: Aeolus Science Conference 2023, 22–26 May 2023, Rhodos, Griechenland, 2023.

Marseille, G.-J., Stoffelen, A., and Barkmeijer, J.: Impact assessment of prospective spaceborne Doppler wind lidar observation scenarios, Tellus A, 60, 234–248, 2008.

Martin, A., Weissmann, M., Reitebuch, O., Rennie, M., Geiß, A., and Cress, A.: Validation of Aeolus winds using radiosonde observations and numerical weather prediction model equivalents, Atmos. Meas. Tech., 14, 2167–2183, https://doi.org/10.5194/amt-14-2167-2021, 2021.

McKay, J. A.: Assessment of a multibeam Fizeau wedge interferometer for Doppler wind lidar, Appl. Opt., 41, 1760–1767, 2002.

Meyer, Y.: Fringe shape with an interferential wedge, JOSA, 71, 1255–1263, 1981.

Olivero, J. J. and Longbothum, R.: Empirical fits to the Voigt line width: A brief review, J. Quant. Spectrosc. Ra., 17, 233–236, 1977.

Reitebuch, O.: The Spaceborne Wind Lidar Mission ADM-Aeolus, in: Atmospheric Physics: Background – Methods – Trends, edited by: Schumann, U., Springer Berlin, Heidelberg, p. 877, https://doi.org/10.1007/978-3-642-30183-4_49, 2012.

Reitebuch, O., Lemmerz, C., Nagel, E., Paffrath, U., Durand, Y., Endemann, M., Fabre, F., and Chaloupy, M.: The Airborne Demonstrator for the Direct-Detection Doppler Wind Lidar ALADIN on ADM-Aeolus. Part I: Instrument Design and Comparison to Satellite Instrument, J. Atmos. Ocean. Tech., 26, 2501–2515, 2009.

Reitebuch, O., Huber, D., and Nikolaus, I.: Algorithm Theoretical Basis Document ATBD: ADM-Aeolus Level 1B Products, Tech. rep., AE-RP-DLR-L1B-001, 2014.

Reitebuch, O., Huber, D., and Nikolaus, I.: ADM-Aeolus Algorithm Theoretical Basis Document (ATBD) – Level 1B products, AE.RP.DLR.L1B.001, p. 117, 2018.

Reitebuch, O., Lemmerz, C., Lux, O., Marksteiner, U., Rahm, S., Weiler, F., Witschas, B., Meringer, M., Schmidt, K., Huber, D., Nikolaus, I., Geiss, A., Vaughan, M., Dabas, A., Flament, T., Stieglitz, H., Isaksen, L., Rennie, M., de Kloe, J., Marseille, G.-J., Stoffelen, A., Wernham, D., Kanitz, T., Straume, A.-G., Fehr, T., von Bismark, J., Floberghagen, R., and Parrinello, T.: Initial assessment of the performance of the first Wind Lidar in space on Aeolus, in: EPJ Web Conf., 237, 01010, https://doi.org/10.1051/epjconf/202023701010, 2020.

Reitebuch, O., Krisch, I., Lemmerz, C., Lux, O., Schmidt, K., Witschas, B., Marksteiner, U., Rennie, M., Nikolaus, I., Fabre, F., Trapon, D., Dabas, A., Donovan, D., van Zadelhoff, G.-J., Wang, P., Marseille, G.-J., Kuijt, A., Tagliacarne, F., Perron, G., Huber, D., Meringer, M., Reissig, K., de Kloe, J., Cardaci, M., Gostinicchi, G., McLean, W., Henry, K., Benedetti, A., Bley, S., Stoffelen, A., Sabbatini, P., Mahfouf, J.-F., and Pourret, V.: The Earth Explorer Mission Aeolus for atmospheric wind observations – Final report from the Aeolus Data Innovation and Science Clus-

ter DISC of Phase E, Tech. rep., https://elib.dlr.de/209970/ (last access: 15 April 2025), 2024.

Rennie, M. and Isaksen, L.: The NWP impact of Aeolus Level-2B Winds at ECMWF, ECMWF – ESA Contract Report, WP-5500, Aeolus DISC (data Innovation Science Cluster) Phase E2, 2024.

Rennie, M. P., Isaksen, L., Weiler, F., de Kloe, J., Kanitz, T., and Reitebuch, O.: The impact of Aeolus wind retrievals on ECMWF global weather forecasts, Q. J. Roy. Meteor. Soc., 147, 3555–3586, https://doi.org/10.1002/qj.4142, 2021.

Rye, B. J.: Molecular Backscatter Heterodyne Lidar: A Computational Evaluation, Appl. Opt., 37, 6321–6328, 1998.

Schillinger, M., Morancais, D., Fabre, F., and Culoma, A.: ALADIN: the LIDAR instrument for the AEOLUS mission, in: Sensors, Systems, and Next-Generation Satellites VI, 4881, 40–51, SPIE, https://doi.org/10.1117/12.463024, 2003.

Schröder, T., Lemmerz, C., Reitebuch, O., Wirth, M., Wührer, C., and Treichel, R.: Frequency jitter and spectral width of an injection-seeded Q-switched Nd: YAG laser for a Doppler wind lidar, Appl. Phys. B, 87, 437–444, 2007.

Stoffelen, A., Pailleux, J., Källén, E., Vaughan, J. M., Isaksen, L., Flamant, P., Wergen, W., Andersson, E., Schyberg, H., Culoma, A., Meynart, R., Endemann, M., and Ingmann, P.: The atmospheric dynamics mission for global wind field measurement, B. Am. Meteor. Soc., 86, 73–88, 2005.

Stolz, C. J., Taylor, J. R., Eickelberg, W. K., and Lindh, J. D.: Effects of vacuum exposure on stress and spectral shift of high reflective coatings, Appl. Opt., 32, 5666–5672, https://doi.org/10.1364/AO.32.005666, 1993.

Straume, A.-G., Rennie, M., Isaksen, L., de Kloe, J., Marseille, G.-J., Stoffelen, A., Flament, T., Stieglitz, H., Dabas, A., Huber, D., Reitebuch, O., Lemmerz, C., Lux, O., Marksteiner, U., Rahm, S., Weiler, F., Witschas, B., Meringer, M., Schmidt, K., Nikolaus, I., Geiss, A., Flamant, P., Kanitz, T., Wernham, D., von Bismark, J., Bley, S., Fehr, T., Floberghagen, R., and Parrinello, T.: ESA's Space-based Doppler Wind Lidar Mission Aeolus – First Wind and Aerosol Product Assessment Results, in: EPJ Web Conf., 237, 1007, https://doi.org/10.1051/epjconf/202023701007, 2020.

Tan, D. G., Andersson, E., Fisher, M., and Isaksen, L.: Observing-system impact assessment using a data assimilation ensemble technique: application to the ADM-Aeolus wind profiling mission, Q. J. Roy. Meteor. Soc., 133, 381–390, 2007.

The Pierre Auger Collaboration, Lux, O., Krisch, I., Reitebuch, O., Huber, D., Wernham, D., and Parrinello, T.: Ground observations of a space laser for the assessment of its in-orbitperformance, Optica, 11, 263–272, https://doi.org/10.1364/OPTICA.507619, 2024.

Tudor Davies, J. and Vaughan, J. M.: A New Tabulation of the Voigt Profile, Astrophys. J., 137, 1302, https://doi.org/10.1086/147606, 1963.

Vaughan, J. M.: The Fabry-Perot Interferometer, Adam Hilger, ISBN 0-85274-138-3, 1989.

Vaughan, J. M. and Ridley, K.: Wave optic analysis of Fizeau fringes with plate defects, in: Proceedings of the 17th Coherent Laser Radar Conference, Barcelona, Spain, 17–20 June 2013, 2013.

Vaughan, M. and Ridley, K.: Rigorous Wave Optic Modelling of ALADIN Spectrometers and Performances, Final Report Contract No. 5401002470, European Space Agency (ESA), Noordwijk, the Netherlands, 102, 2016.

Wang, P., Donovan, D. P., van Zadelhoff, G.-J., de Kloe, J., Huber, D., and Reissig, K.: Evaluation of Aeolus feature mask and particle extinction coefficient profile products using CALIPSO data, Atmos. Meas. Tech., 17, 5935–5955, https://doi.org/10.5194/amt-17-5935-2024, 2024.

Weiler, F., Kanitz, T., Wernham, D., Rennie, M., Huber, D., Schillinger, M., Saint-Pe, O., Bell, R., Parrinello, T., and Reitebuch, O.: Characterization of dark current signal measurements of the ACCDs used on board the Aeolus satellite, Atmos. Meas. Tech., 14, 5153–5177, https://doi.org/10.5194/amt-14-5153-2021, 2021.

Weissmann, M. and Cardinali, C.: Impact of airborne Doppler lidar observations on ECMWF forecasts, Q. J. Roy. Meteor. Soc., 133, 107–116, 2007.

Witschas, B.: Analytical model for Rayleigh–Brillouin line shapes in air, Appl. Opt., 50, 267–270, 2011a.

Witschas, B.: Analytical model for Rayleigh–Brillouin line shapes in air: errata, Appl. Opt., 50, 5758–5758, 2011b.

Witschas, B.: Light scattering on molecules in the Atmosphere, in: Atmospheric Physics: Background – Methods – Trends, edited by: Schumann, U., p. 877, Springer Berlin, Heidelberg, https://doi.org/10.1007/978-3-642-30183-4, 2012.

Witschas, B., Vieitez, M. O., van Duijn, E.-J., Reitebuch, O., van de Water, W., and Ubachs, W.: Spontaneous Rayleigh–Brillouin scattering of ultraviolet light in nitrogen, dry air, and moist air, Appl. Opt., 49, 4217–4227, 2010.

Witschas, B., Rahm, S., Dörnbrack, A., Wagner, J., and Rapp, M.: Airborne wind lidar measurements of vertical and horizontal winds for the investigation of orographically induced gravity waves, J. Atmos. Ocean. Tech., 34, 1371–1386, 2017.

Witschas, B., Lemmerz, C., Geiß, A., Lux, O., Marksteiner, U., Rahm, S., Reitebuch, O., and Weiler, F.: First validation of Aeolus wind observations by airborne Doppler wind lidar measurements, Atmos. Meas. Tech., 13, 2381–2396, https://doi.org/10.5194/amt-13-2381-2020, 2020.

Witschas, B., Lemmerz, C., Geiß, A., Lux, O., Marksteiner, U., Rahm, S., Reitebuch, O., Schäfler, A., and Weiler, F.: Validation of the Aeolus L2B wind product with airborne wind lidar measurements in the polar North Atlantic region and in the tropics, Atmos. Meas. Tech., 15, 7049–7070, https://doi.org/10.5194/amt-15-7049-2022, 2022a.

Witschas, B., Lemmerz, C., Lux, O., Marksteiner, U., Reitebuch, O., Weiler, F., Fabre, F., Dabas, A., Flament, T., Huber, D., and Vaughan, M.: Spectral performance analysis of the Aeolus Fabry–Pérot and Fizeau interferometers during the first years of operation, Atmos. Meas. Tech., 15, 1465–1489, https://doi.org/10.5194/amt-15-1465-2022, 2022b.

Witschas, B., Gisinger, S., Rahm, S., Dörnbrack, A., Fritts, D. C., and Rapp, M.: Airborne coherent wind lidar measurements of the momentum flux profile from orographically induced gravity waves, Atmos. Meas. Tech., 16, 1087–1101, https://doi.org/10.5194/amt-16-1087-2023, 2023a.

Witschas, B., Vaughan, M., Lux, O., Lemmerz, C., Nikolaus, I., and Reitebuch, O.: Verification of different Fizeau fringe analysis algorithms based on airborne wind lidar data in support of ESA's Aeolus mission, Appl. Opt., 62, 7917–7930, https://doi.org/10.1364/AO.502955, 2023b.

Remarks from the typesetter

TS1   Is "$A * (v\prime)$" somewhere else in the paper to find? If not, it should be reviewed by the editor before being implemented in the proofreading stage. Please reassess if these changes are strictly necessary before taking this step. For more information, please see our proofreading guidelines at: http://publications.copernicus.org/for_authors/proofreading_guidelines. html. If you want us to change the equations, please prepare an explanatory document (doc or pdf) which we can send to the editor via our system.